DEVELOPMENT OF COMPUTATIONAL METHODS FOR THE ANALYSIS OF AV BIOMECHANICS: A MULTISCALE APPROACH

Doctoral Dissertation of:
Giovanni Rossini

Supervisors:
Prof. Alberto Redaelli
Prof. Emiliano Votta

Tutor:
Prof. Paolo Ravazzani

The Chair of the Doctoral Program:
Prof. Andrea Aliverti

14 November 2019

To my parents, which imparted to me the high value of education

Contents

Abstract

The high prevalence of cardiac diseases and the corresponding social and economical burden has been motivating great efforts in the study of the patho-physiology of the heart and in the development of innovative clinical solutions to cardiac diseases. In particular, a massive research activity has been focusing on the aortic valve (AV), either to understand the physiological behavior (Chandran and Vigmostad (2013), Conti et al. (2010), Votta et al. (2017)) and the mechanisms underlying pathological processes (e.g. calcification of aortic valve leaflets leading to aortic stenosis) (Oomen et al. (2016), Arzani and Mofrad (2017)). In this context, subject-specific geometrical models represent nowadays the last generation of AV finite element (FE) models and are based on the complete 3D reconstruction of patient-specific anatomies through the segmentation of clinical images (Votta et al. (2017), Auricchio et al. (2014)). However, despite substantial advancements in simulation technology, critical heart valve pathological issues remain unsolved. This is mainly due to the fact that, while numerical AV studies have been mostly focused on the organ length-scale, the mechanisms of their pathologies lie mainly in the behaviors of the constituent leaflet tissues and cells. That is, while organ level simulations can assist in understanding how the valve dynamically responds over the cardiac cycle, valve failure are a direct result of poorly understood degenerative processes. Therefore, research projects trying to understand how the deeply studied organ scale mechanical behavior is translated down to the cell scale, and how this stress/strain field impacts the valve interstitial cells (VICs) matrix maintaining role, will be of great significance in the next future. Despite a considerable number of works have been published studying the AV mechanical behavior at a specific length scale, i.e only the tissue one (Bakhaty et al. (2017), Rego and Sacks (2017)), or just the cell one (Sakamoto et al. (2016), Huang et al. (2007)), few works have been published showing a comprehensive multiscale analysis. However, none of the works published on the multiscale analysis includes patient specific geometries at the or-

i

gan scale, leaving an uncovered aspect in this research field. Moreover, subject-specific organ length-scale models, should be enriched with complementary information other than simple anatomical features. Apart from the geometry, the second most important aspect playing a fundamental role in the behavior of the AV is the mechanical property of the tissues. In fact, AV tissues are not only hyperelastic, but strongly anisotropic and inhomogeneous (Billiar and Sacks (2000), Stella and Sacks (2007)). The fibrous architecture is what dictates the direction and degree of mechanical anisotropy, as well as the overall elastic response, and it has therefore to be included in the modeling process in a reliable way.

Hence, starting from the limitations that are still hampering this technique, the aims and scopes of this PhD project were defined to follow the research directions shared in literature in the attempt of pursuing a more subject-specific, complete and reliable numerical description on the multiscale biomechanical behavior of the AV.

First, the project focused on the development of a semi-automated algorithm to generate patient-specific image-based AV FE models for the simulation of the organ length-scale behavior of the AV, including the possibility to set the space-dependent patterns of leaflets thickness, with the aim of comparing different leaflet discretization approaches. Results computed highlighted that the use of solid elements lead to a more reliable quantification of leaflet stresses. Moreover, it was evident that leaflet stresses strongly depend on the local leaflet thickness, thus suggesting that a reliable quantification of the patient-specific tissue thickness distribution should be mandatory in this context.

Second, we developed a FE workflow for the multiscale analysis of the AV biomechanics, starting from subject-specific anatomies able to transfer subject-specific macroscopic features down to the cell length-scale. Thanks to this novel workflow, with the aim of studying the impact of subject-specific organ scale features on the cell-scale mechanical response, we investigated the behavior of the AV leaflets at the organ, tissue and cell length scale. The computed results suggests that the organization of matrix within the valve tissue acts to reduce direct tensile strain transfer to cells in the circumferential direction, while the radial directions appears as the one which is more sensible to anatomical leaflet differences.

Lastly, in a project carried out in collaboration with the research group of Prof. M. S. Sacks at the Willerson Center for Cardiovascular Modeling and Simulation (Austin, Texas, USA), we developed a novel structural tensor method to describe fiber orientation probability density functions (ODFs), allowing for an efficient representation and tensor coordinate

transformation to facilitate fibers architecture mapping from experimental data to NURBS based representations of AV leaflet geometry. We demonstrated the efficacy of this innovative approach starting from human derived small angle light scattering (SALS) structural experimental data.

To conclude, this project tackled different aspects of numerical FE modeling of AV, focusing on the attention to the modelling and discretization aspects, the development of a subject-specific multiscale approach going from the organ down to the cell length-scale, and the inclusion of structural tissue information in the organ length-scale models. Novel solutions were implemented to advance the current state of the art, focusing, in particular, on those technological and methodological issues that are still hampering a more comprehensive description of the biomechanical behavior of the AV through numerical simulations.

Bibliography

Arzani, A. and Mofrad, M. R. (2017). A strain-based finite element model for calcification progression in aortic valves. *Journal of Biomechanics*, 65:216–220.

Auricchio, F., Conti, M., Morganti, S., and Reali, A. (2014). Simulation of transcatheter aortic valve implantation: a patient-specific finite element approach. *Computer Methods in Biomechanics and Biomedical Engineering*, 17(12):1347–1357.

Bakhaty, A. A., Govindjee, S., and Mofrad, M. R. (2017). Consistent tri-layer biomechanical modeling of aortic valve leaflet tissue. *Journal of Biomechanics*, 61:1–10.

Billiar, K. L. and Sacks, M. S. (2000). Biaxial mechanical properties of the natural and glutaraldehyde treated aortic valve cusp–Part I: Experimental results. *Journal of biomechanical engineering*, 122(1):23–30.

Chandran, K. B. and Vigmostad, S. C. (2013). Patient-specific bicuspid valve dynamics: Overview of methods and challenges. *Journal of Biomechanics*, 46(2):208–216.

Conti, C. A., Votta, E., Della Corte, A., Del Viscovo, L., Bancone, C., Cotrufo, M., and Redaelli, A. (2010). Dynamic finite element analysis of the aortic root from MRI-derived parameters. *Medical Engineering and Physics*, 32(2):212–221.

Huang, H. Y. S., Liao, J., and Sacks, M. S. (2007). In-situ deformation of the aortic valve interstitial cell nucleus under diastolic loading. *Journal of Biomechanical Engineering*, 129(6):880–889.

Oomen, P., Loerakker, S., van Geemen, D., Neggers, J., Goumans, M.-J., van den Bogaerdt, A., Bogers, A., Bouten, C., and Baaijens, F. (2016). Age-dependent changes of stress and strain in the human heart valve and their relation with collagen remodeling. *Acta Biomaterialia*, 29:161–169.

Rego, B. V. and Sacks, M. S. (2017). A functionally graded material model for the transmural stress distribution of the aortic valve leaflet. *Journal of Biomechanics*, 54:88–95.

Sakamoto, Y., Buchanan, R. M., and Sacks, M. S. (2016). On intrinsic stress fiber contractile forces in semilunar heart valve interstitial cells

using a continuum mixture model. *Journal of the Mechanical Behavior of Biomedical Materials*, 54:244–258.

Stella, J. A. and Sacks, M. S. (2007). On the Biaxial Mechanical Properties of the Layers of the Aortic Valve Leaflet. *Journal of Biomechanical Engineering*, 129(5):757.

Votta, E., Presicce, M., Della Corte, A., Dellegrottaglie, S., Bancone, C., Sturla, F., and Redaelli, A. (2017). A novel approach to the quantification of aortic root in vivo structural mechanics. *International Journal for Numerical Methods in Biomedical Engineering*, 33(9):1–22.

Chapter 1

Introduction

1.1 Background

1.1.1 Cardiovascular system

The cardiovascular system consists of a closed circuit composed of arteries, arterioles, capillaries, venules, veins and the heart. Blood flow within the cardiovascular system is guided by the mechanical force exerted by the heart, which muscle fibers alternatively contract and relax to push blood towards peripheral vessels and to allow its passive return. From a func-
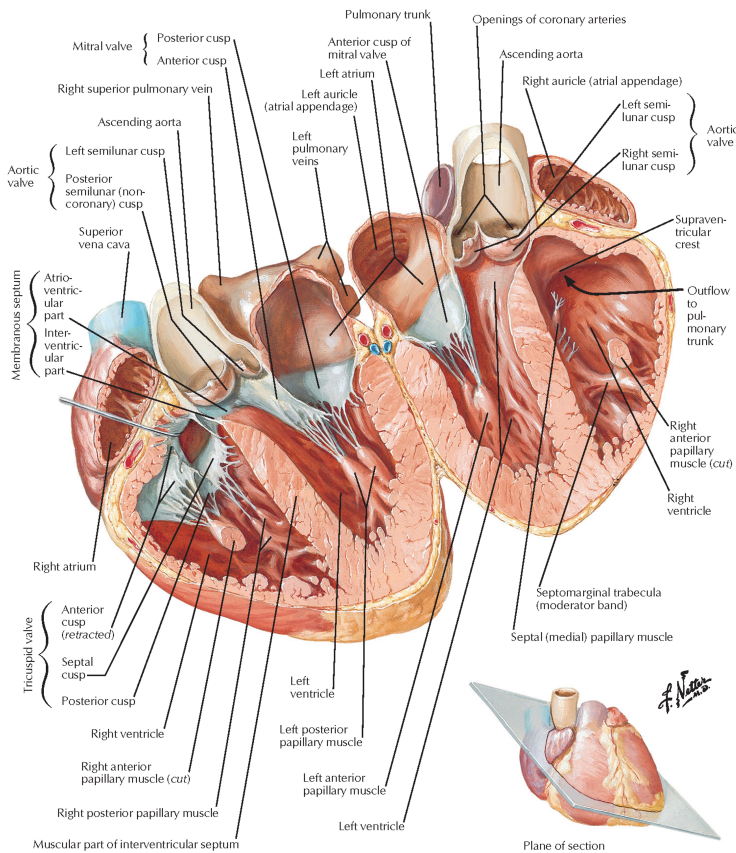
Figure 1.1: *Illustration of the heart in a section-view. All the relevant structures at the organ-length scale are reported and detailed. Adapted from Netter (2014)*

tional standpoint, the heart consists of two pulsatile volumetric pumps in series. Each of them consists of two connected chambers: the atrium, which is located superiorly, receives blood from the veins and successively

moves it into the second cavity, i.e. the ventricle, which is located inferiorly and pumps blood in the arteries that supply the organs within the body (Figure 1.1). Namely, the right ventricle pumps the blood to the lungs through the pulmonary arteries, while the left ventricle pumps the blood to all of the body peripheral systems through the aorta and the corresponding branches; the right and left hearts are separated by a wall called septum. Between each atrium and the corresponding ventricle there is an atrioventricular valve that allows for the unidirectional blood flow from the former latter. The atrioventricular valve is called tricuspid valve (i.e. with three leaflets) and mitral valve (with two leaflets) in the right and left heart, respectively. Between each ventricle and the corresponding outgoing vessel there is a semilunar valve that guarantees the blood unidirectional flow out of the heart. The semilunar valve is called pulmonary and aortic valve in the right and left heart, respectively, owing to the artery connected to the valve. Both these valves are made of three leaflets. The opening and closure of the valves are mostly a passive phenomena driven by pressure differences between the upstream and downstream compartments separated by the valve. Based on such pressure differences, and hence on the valves closed or open configuration, the cardiac cycle characterizing heart function can be divided in three functional phases:

- *atrial diastole*: atrioventricular valves are closed to allow for the filling of the atrial with the blood coming from the pulmonary veins (left atrium) and venae cavae (right atrium); pressure increases along with atrium filling.

- *atrial systole and ventricular diastole*: atrioventricular valves open under the atrial pressure and blood flows from the two atria to the two ventricles filling them completely. When the ventricular pressure exceeds the atrial pressure the atrioventricular valves close again to prevent from atrial regurgitation.

- *ventricular systole*: the ventricular wall undergo a fast contraction and the ventricular pressure increases fast (isovolumetric contraction). When pressure in the left ventricle exceeds the aortic pressure ($80\,\mathrm{mmHg}$) and pressure in the right ventricle exceeds the pulmonary artery pressure ($8\,\mathrm{mmHg}$) the two semilunar valves open allowing for blood ejection. Subsequently, the ventricular pressure starts to decrease to the diastolic levels and a new cardiac cycle starts.

1.1.2 Organ-scale length AV anatomy

The aortic valve is located inside the aortic root (AR) which is the functional and anatomical unit connecting the outlet of left ventricle to the ascending aorta. The aortic wall encompassing the aortic root can be divided in two main portions: a tri-lobated bulb, consisting of the three Valsalva sinuses, and the tubular ascending aorta, which represents the most distal portion of the aortic root. The Valsalva sinuses are called left-coronary, right-coronary and non-coronary, based on their position and on the fact that two sinuses each contain the orifice of a main arterial coronary. The whole AR structure is located in close proximity of the two atrioventricular valves. In particular, the non-coronary and left-coronary leaflets of the aortic valve face the mitral valve (Figure 1.2). From the structural point of
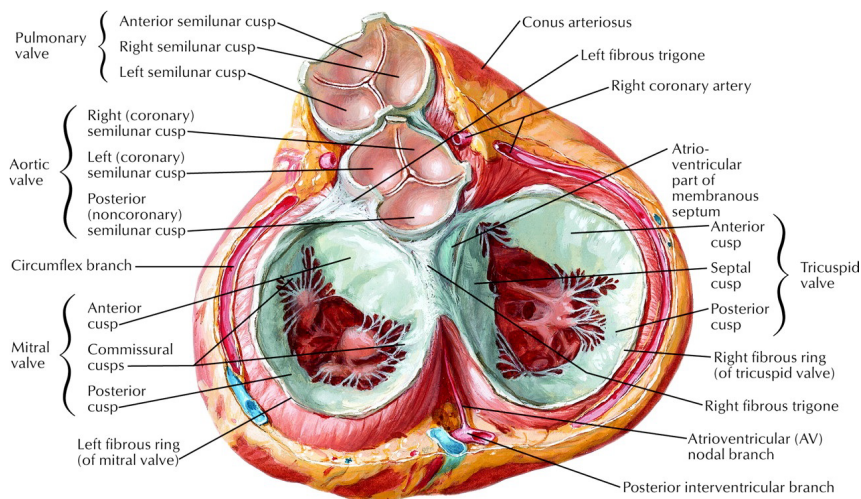
Figure 1.2: *Valvular plane as seen from the atrial side; valves are represented in their diastolic configuration.Three aortic valve leaflets and their respective positions are clearly visible: RC leaflet (right-coronary), LC leaflet (left-coronary) and NC leaflet (non-coronary). Adapted from Netter (2014)*

view, the aortic valve (AV) is composed by three leaflets classified as the Valsalva sinuses: left-coronary (LC), right-coronary (RC), non-coronary (NC). In each leaflet, the line of insertion is longer than their free margin. Each leaflet covers approximately one third of aortic valve orifice. Within each leaflet, four regions are usually identified (Underwood (2000)) (Figure 1.3):

- *basal region*: it is located all along the insertion line of the leaflet and

runs from commissure to commissure. It is characterized by an high density of fibrous collagen tissue.

- *belly region*: it is the central portion of the leaflet, as well as the widest and thinnest of the four regions. When inspected, this region is almost transparent.

- *coaptation region*: the portion of the leaflet that gets in contact with the complementary leaflets when the valve is closed, i.e. during ventricular diastole.

- *free margin*: it's the free boundary of the leaflet. The central point of this region is characterized by the so-called nodulus of Arantius, i.e. a thicker and almost spherical anatomical feature that helps achieving the full continence of the valve during ventricular diastole.
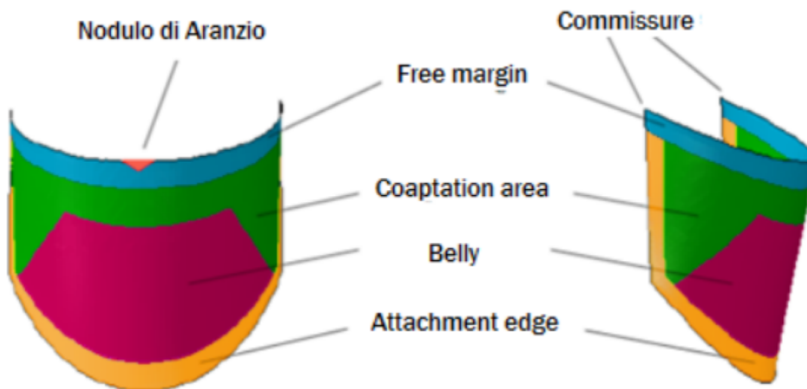
Figure 1.3: *Schematic representation of the four regions of an aortic valve leaflet, as seen from an anterior (left hand panel) and lateral (right hand panel) view.*

1.1.3 Tissue-scale length AV Leaflets Structure

The tissue of aortic leaflets organized into three different layers through the leaflet thickness, whose combined behavior is responsible for the peculiar characteristics of the entire leaflet: very low flexional rigidity, to guarantee a fast opening in systole, and a very high tensile strength, which allows for bearing the important high pressure differences in diastole. The three layers show very different properties and are called laminae (Figure 1.4):

- *lamina fibrosa*: it is the thickest layer (about 40% of the total leaflet thickness, Stella and Sacks (2007)) and covers the entire aortic surface of the leaflet. In this lamina, type I collagen fibers are orientated circumferentially (from commissure to commissure); these are folded in systole, when the tissue undergoes flexion, and stretched in diastole, when the tissue undergoes traction due to the trans-valvular pressure difference.

- *lamina ventricularis*: it is the layer exposed to the ventricle and it account for about 30% of the leaflet thickness (Stella and Sacks (2007)). It contains a dense net of collagen and elastin (Vesely (1997)), where the radially oriented elastin fibers help reducing the radial deformation during the systole, facilitating the transvalvular blood flow.

- *lamina spongiosa*: it is the middle layer and account for about 30% of the total leaflet thickness. It contains many hydrated GAGs and PGs, which serve as lubricant during the relative motion of the other two layers (Rego and Sacks (2017)).
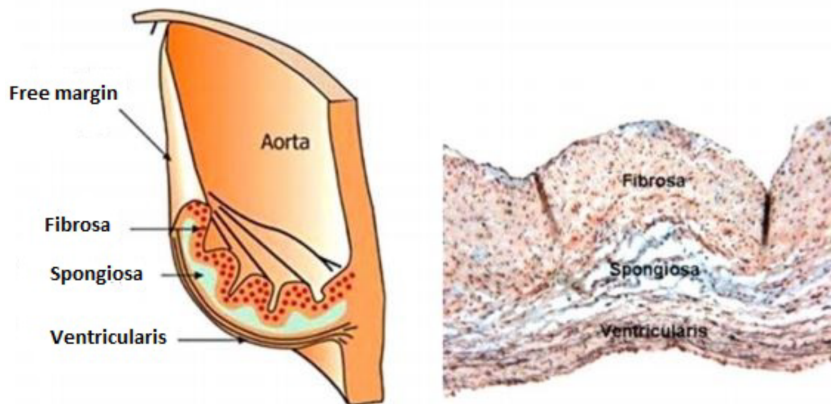
Figure 1.4: *Left hand panel: sketch of an aortic leaflet depicting the three laminae. Right hand panel: histological section of the three laminae in the aortic leaflet.*

The above described micro-structure gives to the aortic leaflets a particular mechanical response with five main characteristics: non homogeneous, elastic (layer structure), anisotropic (preferential directions of the collagen fibers), non-linear (collagen fiber progressive recruitment), and isochoric (water and GAGs presence). Many authors studied the mechanical response of aortic leaflets tissue using biaxial tests (May-Newman et al.

(2009), Billiar and Sacks (2000), Vesely (1997)). The first constitutive model of aortic valve leaflets tissue was formulated by Billiar and Sacks based on load-controlled biaxial tests on human specimens (Billiar and Sacks (2002)). The results yielded by those tests in terms of membrane tension vs real strains in the radial and circumferential directions highlighted marked anisotropy of the tissue. In particular,the mechanical response in the circumferential directions is much stiffer than the response in the radial one Figure 1.5). Indeed, the peak strain differs by more than 30% between the two directions.
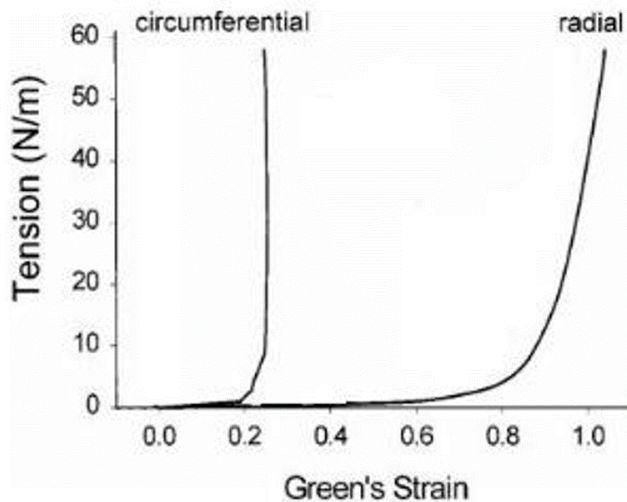
Figure 1.5: *Representative circumferential and radial stress-strain curves from a fresh and a glutaraldehyde-fixed AV cusp, which show the pronounced mechanical anisotropy of both tissues Billiar and Sacks (2000)*

1.1.4 Cell-scale length AV Micro-structure

The ventricular side of the ventricularis layer and the aortic side of the fibrosa layer are covered by valve endothelial cells (VECs), which maintain valve homeostasis by regulating permeability, inflammatory cell adhesion, and paracrine signaling. Valve interstitial cells populate the fibrosa (Figure 1.6), spongiosa and ventricularis extracellular matrix (ECM); this cells are of particular interest because they play en essential role in the matrix maintenance, with VIC dysfunction implicated as the underlying cause of many heart valve diseases (Sakamoto et al. (2016)), e.g. calcific aortic valve.
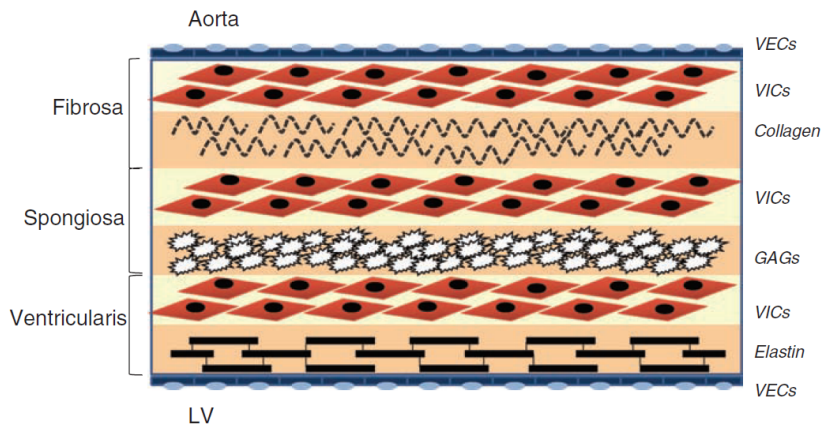
Figure 1.6: *Cellular architecture of the aortic valve. Valve endothelial cells (VECs) on the outer surface (both on the aortic and ventricular side), and valve interstitial cells (VICs) in the layers bulk Zhiduleva et al. (2018).*

1.2 AV numerical simulations: state of the art

The high prevalence of cardiac diseases and the corresponding social and economical burden has been motivating great efforts in the study of the patho-physiology of the heart and in the development of innovative clinical solutions to cardiac diseases. In particular, a massive research activity has been focusing on the AV, either to understand the physiological behavior (Chandran and Vigmostad (2013), Conti et al. (2010), Votta et al. (2017)) and the mechanisms underlying pathological processes (e.g. calcification of aortic valve leaflets leading to aortic stenosis) (Oomen et al. (2016), Arzani and Mofrad (2017)) or to analyze the effects of surgical and interventional procedures (e.g. valve sparing techniques, and trans-catheter aortic valve implantation) (Sturla et al. (2016), Bianchi et al. (2019)). In this context, the continuous increase in computational power of microprocessors and in availability of parallel or distributed computing systems has boosted the exploitation of numerical simulations to aid research on the AV. The most widely used numerical models mainly rely on two different approach, namely the finite element (FE) and the finite volume theories. The former is used in finite element analysis (FEA), and it is suitable for structural problem where the presence of the fluid is neglected and its effect is accounted for by means of equivalent pressure loading boundaries; the latter is exploited in the computational fluid dynamics (CFD) studies. In either case, the initial geometry, as a complex domain, is subdivided into

smaller, simpler ones (*discretization*), so the governing partial differential equation (PDE) problem can be approximated with system of algebraic or ordinary differential equations. Then, defining the proper physical material properties, boundary and loading conditions, such method allows for the evaluation of several field variables which cannot be directly computed or measured through any experimental tool, mainly bulk strain and stress fields for FEA and velocity/pressure field or shear stress for CFD. Higher is the level of detail in the problem modeling, more accurate will be the solution, as well as greater will be also the computational cost.

However, focusing on FEA, the implementation of a fully realistic FE model of a cardiac district still represents a challenging task, because of the high complexity of the issues to be addressed at once, namely the morphology, the tissue mechanical response, the dynamic loading and boundary conditions and the interaction with the surrounding structures. Reviewing the literature, in the last decade, developments in this specific type of activity focused on merging image processing techniques, starting directly from clinical imaging acquisitions, and FEA to quantify the structural response of the AV through so called subject-specific models.

In fact, together with the development and optimization of numerical simulations techniques, much of the recent advancement in valvular heart disease evaluation can be attributed to the advent of noninvasive cardiac imaging modalities, such as echocardiography, cMRI and CT, which are now being used extensively for diagnostics and risk evaluation (Sun et al. (2014)). In particular, 3D volumetric acquisition enables the visualization of cardiac districts from virtually any perspective, better appreciating patient-specific anatomical complexity and carrying some indisputable advantages if compared to more "classic" 2D acquisition techniques. Furthermore, considering the dynamically changing configuration of the cardiac structures within the cardiac cycle, one should be aware of the relevance of introducing 4-dimension information, namely the time (Caiani et al. (2011)). Dynamic 3D imaging, such as real-time 3D echocardiography, 4D CT and cMRI can be crucial in the assessment of the spatial and functional relationship of an anatomical district with surrounding tissues, such as the left ventricle outflow tract and mitral annulus or the AV complex itself (Muraru et al. (2012), Elattar et al. (2017)). These features can be beneficial in applications requiring real-time imaging and response, such as 3D image-guided cardiac procedures (Kasel et al. (2013)). In addition, volumetric data can be used to obtain 3D patient-specific computational models of the cardiac valves, which can be exploited for FE biomechanical analysis.

In the following sections we present the current state of the art and the

9

most important actual limitations regarding the subject-specific analysis of the AV biomechanics.

1.2.1 Subject-specific AV FEA

The customization of healthcare, with medical decisions, treatments, practices, or products being tailored to the individual patient is forecast to be the next step in medicine (Collins and Varmus (2015)); therefore, also numerical models of anatomical district, such as AV, are expected to move towards the replication of all the variable of interest in a subject-specific manner, to achieve results and indications which may be relevant for the clinical practice in the most reliable way. Before the development of this subject-specific models, paradigmatic models were the standard in FEA of AV. These models relied on very simple geometries built using dimensions and proportions from ex-vivo AVs excised from animals (Gnyaneshwar and Kumar (2002)) of using population averaged measurement from clinical images (Conti et al. (2010)). This model are useful tools to study a general response of the AV anatomical district or to investigate how a specific device works, but it's obviously impossible to derive information that are subject-specific. Therefore several groups started working towards an AV FEA able to include detailed anatomical features, and several papers have been published in literature in the last decades. Subject-specific geometrical models represent nowadays the last generation of AV FE models and are based on the complete 3D reconstruction of patient-specific anatomies through the segmentation of clinical images (Votta et al. (2017), Auricchio et al. (2014)). Contrarily to paradigmatic geometries, subject-specific models offer the possibility to make inference from the simulation results which are specific for the AV of interest, pushing this field of research more and more close to a direct clinical application. However, despite these substantial advancements in simulation technology, critical heart valve pathological issues remain unsolved. This is mainly due to the fact that, while numerical AV studies have been mostly focused on the organ length-scale, the mechanisms of their pathologies lie mainly in the behaviors of the constituent leaflet tissues and cells. That is, while organ level simulations can assist in understanding how the valve dynamically responds over the cardiac cycle, valve failure are a direct result of poorly understood degenerative processes. Therefore, research projects trying to understand how the deeply studied organ scale mechanical behavior is translated down to the cell scale, and how this stress/strain field impacts the VICs matrix maintaining role, will be of great significance in the next future. Despite a con-

siderable number of works have been published studying the AV mechanical behavior at a specific length scale, i.e only the tissue one (Bakhaty et al. (2017), Rego and Sacks (2017)), or just the cell one (Sakamoto et al. (2016), Huang et al. (2007)), few works have been published showing a comprehensive numerical multiscale analysis not only of the AV, but of all heart valves in general (Weinberg and Mofrad (2007), Weinberg et al. (2010)). Among them the first, most complete and still the reference in this sector is the one published by Weinberg and Mofrad (2007). The authors propose a complete multiscale FE workflow going from the organ length-scale down to the cell length-scale, passing through the tissue length-scale. However, none of the works published on the multiscale analysis includes subject-specific geometries at the organ scale, leaving an uncovered aspect in this research field. Moreover, subject-specific organ length-scale models, which should represent the starting point for such a multiscale approach, have to be enriched with complementary information other than simple anatomical features, e.g. leaflet shape and extent, the commissure position and the leaflet thickness. Apart from the geometry, the second most important aspect playing a fundamental role in the behavior of the AV is the mechanical property of the tissues. As abovementioned, AV tissues are not only hyperelastic, but strongly anisotropic and inhomogeneous (Billiar and Sacks (2000), Stella and Sacks (2007)). The fibrous architecture is what dictates the direction and degree of mechanical anisotropy, as well as the overall elastic response. A reliable fiber architecture representation has a strong impact not only at the organ length-scale, but down to the tissue and cell length-scales. The presence of collagen fibers have been included as a parameter in several mechanical models (Bakhaty et al. (2017), Arzani and Mofrad (2017), Sturla et al. (2016)); however, in these models the fiber direction was set to fit biaxal experimental data derived from samples. This means that the fiber structure is somehow hidden in the model and the need of a more imaged-based fiber structure inclusion in mechanical models is still an open issue.

1.2.2 Current limitations

Despite the advancement in the accuracy and reliability of subject-specific numerical modeling of AV and the increasing not only in the number, but also in the level of detail in these type of studies, a number of hurdles and limitations yet exist. Still, many efforts need to be made in order to develop a complete understanding of the AV biomechanical behavior at all its length-scale and not only at the organ one. In fact, few works studying

the heart valves biomechanics under a complete multiscale perspective, i.e. not only focusing on one specific length-scale, are present in literature (Lee et al. (2015), Weinberg and Mofrad (2007)). The latter represent in our opinion the first and most important limitation in the field of AV FE models; in fact, as above-mentioned, while organ level simulations can assist in understanding how the valve dynamically responds over the cardiac cycle, valve degeneration and failure are a direct result of degenerative processes taking place at a lower level. Therefore, it is mandatory to find a solid way to translate biomechanical information among different AV length scale. The second main limitation directly derive from the direction of the multi-scale simulation workflow, which goes from the "observable" organ length-scale to the "hidden" cell length-scale. This course need the most precise and complete description at the organ length-scale, which is the first one to be simulated, in order to avoid the introduction of errors and inaccuracies at the lower length-scales, i.e. the tissue and the cell ones. Despite the fact that the AV organ-length scale biomechanics is the most widely studied among the three length-scales, some improvement are still possible. In particular, an efficient way to include collagen fiber macroscopic structure information at the organ length-scale on a patient-specif geometry starting directly from experimental data is still missing. However, the inclusion of such information could pave the way for a clear investigation of the impact of macroscopic mechanical stimuli and structure on the matrix maintaining role of VICs and therefore on the tissue remodeling processes, such as AV calcification, which has a direct and strong clinical throwback (Sakamoto et al. (2017)).

1.3 Conclusive remarks

The state of the art presented in the previous sections was intended to give the reader an overview of the current state of the art of numerical FE modeling of AV. Consequently, starting from the limitations that are still hampering this technique, the aims and scopes of the PhD project were defined to follow the research directions shared in literature in the attempt of pursuing a more subject-specific, complete and reliable numerical description on the multiscale biomechanical behavior of the AV.

1.3.1 Aims and scopes

This work was conceived to tackle different aspects related to the limitations of subject-specific FEA of the AV biomechanics described in Sec-

tion 1.2.2. In-house algorithm were developed to obtain a reliable organ length-scale modelling of the AV starting from clinical images; particular attention was given to the discretization method used to describe the leaflet geometry, with the aim of obtaining the most reliable stress-strain pattern in the cross-section leaflet direction. Moreover, the developed modelling technique was expanded in order to build up a complete multiscale FE modeling workflow, with the intent of improve the description of the AV behavior from the organ length-scale down to the cell length-scale including subject-specific anatomical features directly derived from clinical image segmentation. Finally, a novel structural tensor method to represent the collagen fiber structure was developed, using probability density functions (ODFs) starting from experimental data from ex-vivo AV leaflets. In particular, the main aim of this methodology was to obtain a mapping technique allowing to smoothly transfer the in-vitro collagen fiber orientation to any in-vivo measured leaflet geometry, using a workflow which could be later included in the organ length-scale modeling of a multiscale FEA.

1.3.2 Thesis outline

The following part of the thesis is structured as herein detailed:

- Chapter 2. This Chapter describes the development and implementation of a semi-automated algorithm to generate patient-specific image-based AV FE models for the simulation of the organ length-scale behavior of the AV, including the possibility to set the space-dependent patterns of leaflets thickness. Specifically, the workflow was organized into the following steps: acquisition of cMRI data, segmentation and model reconstruction, computation of the pre-stresses and of the AV biomechanics. Through this benchmark we compared the results in term of stress and strain on the leaflet surface and throughout its thickness of different discretization approaches in describing the leaflet geometry.

- Chapter 3. This Chapter describes the development and implementation of a FE workflow for the multiscale analysis of the AV biomechanics, starting from subject-specific anatomies. The modeling workflow consists of three simulations at three different length-scales: organ (cm to mm), tissue (mm) and cell (μm). These are organized in a top-down scheme, so that each simulation provides data to feed the simulation at the immediately smaller length-scale. The workflow was tested on the anatomy from three healthy subjects, with the aim

of investigate how macroscopic anatomical features at the macroscale impact the strain behaved by VICs at the cell scale in the fibrosa layer.

- Chapter 4. This Chapter describes the development of a novel structural tensor method to describe collagen fiber orientation probability density functions (ODFs), allowing for an efficient representation and tensor coordinate transformation to facilitate mapping from experimental data to NURBS based representations of AV leaflet geometry. We demonstrated the efficacy of this innovative approach starting from human derived SALS (Small Angle Light Scattering) structural experimental data from the work of Aggarwal et al. (2014).

- Chapter 5. In the last Chapter, a general discussion of the PhD dissertation and the conclusive remarks are presented.

The activities described in Chapter 4 were carried out in collaboration with the research group of Prof. M. S. Sacks at the Willerson Center for Cardiovascular Modeling and Simulation during an exchange period at UT Austin (Austin, Texas, USA).

Bibliography

Aggarwal, A., Ferrari, G., Joyce, E., Daniels, M. J., Sainger, R., Gorman, J. H., Gorman, R., and Sacks, M. S. (2014). Architectural Trends in the Human Normal and Bicuspid Aortic Valve Leaflet and Its Relevance to Valve Disease. *Annals of Biomedical Engineering*, 42(5):986–998.

Arzani, A. and Mofrad, M. R. (2017). A strain-based finite element model for calcification progression in aortic valves. *Journal of Biomechanics*, 65:216–220.

Auricchio, F., Conti, M., Morganti, S., and Reali, A. (2014). Simulation of transcatheter aortic valve implantation: a patient-specific finite element approach. *Computer Methods in Biomechanics and Biomedical Engineering*, 17(12):1347–1357.

Bakhaty, A. A., Govindjee, S., and Mofrad, M. R. (2017). Consistent trilayer biomechanical modeling of aortic valve leaflet tissue. *Journal of Biomechanics*, 61:1–10.

Bianchi, M., Marom, G., Ghosh, R. P., Rotman, O. M., Parikh, P., Gruberg, L., and Bluestein, D. (2019). Patient-specific simulation of transcatheter aortic valve replacement: impact of deployment options on paravalvular leakage. *Biomechanics and Modeling in Mechanobiology*, 18(2):435–451.

Billiar, K. L. and Sacks, M. S. (2000). Biaxial mechanical properties of the natural and glutaraldehyde treated aortic valve cusp–Part I: Experimental results. *Journal of biomechanical engineering*, 122(1):23–30.

Billiar, K. L. and Sacks, M. S. (2002). Biaxial Mechanical Properties of the Native and Glutaraldehyde-Treated Aortic Valve Cusp: Part IIâA Structural Constitutive Model. *Journal of Biomechanical Engineering*, 122(4):327.

Caiani, E. G., Fusini, L., Veronesi, F., Tamborini, G., Maffessanti, F., Gripari, P., Corsi, C., Naliato, M., Zanobini, M., Alamanni, F., and Pepi, M. (2011). Quantification of mitral annulus dynamic morphology in patients with mitral valve prolapse undergoing repair and annuloplasty during a 6-month follow-up. *European Journal of Echocardiography*, 12(5):375–383.

Chandran, K. B. and Vigmostad, S. C. (2013). Patient-specific bicuspid valve dynamics: Overview of methods and challenges. *Journal of Biomechanics*, 46(2):208–216.

Collins, F. S. and Varmus, H. (2015). A New Initiative on Precision Medicine. *New England Journal of Medicine*, 372(9):793–795.

Conti, C. A., Votta, E., Della Corte, A., Del Viscovo, L., Bancone, C., Cotrufo, M., and Redaelli, A. (2010). Dynamic finite element analysis of the aortic root from MRI-derived parameters. *Medical Engineering and Physics*, 32(2):212–221.

Elattar, M. A., Vink, L. W., van Mourik, M. S., Baan, J., VanBavel, E. T., Planken, R. N., and Marquering, H. A. (2017). Dynamics of the aortic annulus in 4D CT angiography for transcatheter aortic valve implantation patients. *PLOS ONE*, 12(9):e0184133.

Gnyaneshwar, R. and Kumar, R. K. (2002). Original article : cardiovascular Dynamic analysis of the aortic valve using a finite. 73(4):3–6.

Huang, H. Y. S., Liao, J., and Sacks, M. S. (2007). In-situ deformation of the aortic valve interstitial cell nucleus under diastolic loading. *Journal of Biomechanical Engineering*, 129(6):880–889.

Kasel, A. M., Cassese, S., Bleiziffer, S., Amaki, M., Hahn, R. T., Kastrati, A., and Sengupta, P. P. (2013). Standardized Imaging for Aortic Annular Sizing. *JACC: Cardiovascular Imaging*, 6(2):249–262.

Lee, C. H., Carruthers, C. A., Ayoub, S., Gorman, R. C., Gorman, J. H., and Sacks, M. S. (2015). Quantification and simulation of layer-specific mitral valve interstitial cells deformation under physiological loading. *Journal of Theoretical Biology*, 373:26–39.

May-Newman, K., Lam, C., and Yin, F. C. P. (2009). A Hyperelastic Constitutive Law for Aortic Valve Tissue. *Journal of Biomechanical Engineering*, 131(8):081009.

Muraru, D., Badano, L. P., Vannan, M., and Iliceto, S. (2012). Assessment of aortic valve complex by three-dimensional echocardiography: a framework for its effective application in clinical practice. *European Heart Journal - Cardiovascular Imaging*, 13(7):541–555.

Netter, F. (2014). *Atlas of Human Anatomy*. Elsevier, 6th edition.

Oomen, P., Loerakker, S., van Geemen, D., Neggers, J., Goumans, M.-J., van den Bogaerdt, A., Bogers, A., Bouten, C., and Baaijens, F. (2016). Age-dependent changes of stress and strain in the human heart valve and their relation with collagen remodeling. *Acta Biomaterialia*, 29:161–169.

Rego, B. V. and Sacks, M. S. (2017). A functionally graded material model for the transmural stress distribution of the aortic valve leaflet. *Journal of Biomechanics*, 54:88–95.

Sakamoto, Y., Buchanan, R. M., and Sacks, M. S. (2016). On intrinsic stress fiber contractile forces in semilunar heart valve interstitial cells using a continuum mixture model. *Journal of the Mechanical Behavior of Biomedical Materials*, 54:244–258.

Sakamoto, Y., Buchanan, R. M., Sanchez-Adams, J., Guilak, F., and Sacks, M. S. (2017). On the Functional Role of Valve Interstitial Cell Stress Fibers: A Continuum Modeling Approach. *Journal of Biomechanical Engineering*, 139(2):021007.

Stella, J. A. and Sacks, M. S. (2007). On the Biaxial Mechanical Properties of the Layers of the Aortic Valve Leaflet. *Journal of Biomechanical Engineering*, 129(5):757.

Sturla, F., Ronzoni, M., Vitali, M., Dimasi, A., Vismara, R., Preston-Maher, G., Burriesci, G., Votta, E., and Redaelli, A. (2016). Impact of different aortic valve calcification patterns on the outcome of transcatheter aortic valve implantation: A finite element study. *Journal of Biomechanics*, 49(12):2520–2530.

Sun, W., Martin, C., and Pham, T. (2014). Computational Modeling of Cardiac Valve Function and Intervention. *Annual Review of Biomedical Engineering*, 16(1):53–76.

Underwood, M. J. (2000). The aortic root: structure, function, and surgical reconstruction. *Heart*, 83(4):376–380.

Vesely, I. (1997). The role of elastin in aortic valve mechanics. *Journal of Biomechanics*, 31(2):115–123.

Votta, E., Presicce, M., Della Corte, A., Dellegrottaglie, S., Bancone, C., Sturla, F., and Redaelli, A. (2017). A novel approach to the quantification of aortic root in vivo structural mechanics. *International Journal for Numerical Methods in Biomedical Engineering*, 33(9):1–22.

Weinberg, E. J. and Mofrad, M. R. K. (2007). Three-dimensional, multi-scale simulations of the human aortic valve. *Cardiovascular Engineering*, 7(4):140–155.

Weinberg, E. J., Shahmirzadi, D., Mohammad, ·., and Mofrad, R. K. (2010). On the multiscale modeling of heart valve biomechanics in health and disease. *Biomech Model Mechanobiol*, 9:373–387.

Zhiduleva, E. V., Irtyuga, O. B., Shishkova, A. A., Ignat'eva, E. V., Kostina, A. S., Levchuk, K. A., Golovkin, A. S., Rylov, A. Y., Kostareva, A. A., Moiseeva, O. M., Malashicheva, A. B., and Gordeev, M. L. (2018). Cellular Mechanisms of Aortic Valve Calcification. *Bulletin of Experimental Biology and Medicine*, 164(3):371–375.

Chapter 2

Impact of leaflets thickness distribution and discretization approach in AV numerical simulations

2.1   Introduction

With the aim of studying the AV biomechanical behavior, different numerical methods are available in the scientific literature. However, regardless the chosen approach, some main steps are shared between the different works. The quantitative reconstruction of AV geometry represents the first step towards the implementation of a structural model. In terms of geometrical realism, three generations of models can be identified in the literature. The most seminal models relied on a very simple and idealized geometry, as well exemplified by the work of Gnyaneshwar and Kumar (2002) where the geometry was created using the procedure illustrated by Thubrikar in his work on the aortic valve (M. Thubrikar (1979)). This parametric models provides extremely valuable insight and offers the best options for testing solution, but the physiological variability in valve design is not properly elucidated and described and, as a result, this approach seems to be somehow too rigid if the aim is to accommodate the dimensional variability observed in normally functioning valves. The second generation of models still made use of idealized geometrical paradigms, but removed the aforementioned assumptions and used measurements from *in-vivo* images to set the dimensions of AV substructures. For instance, in the the work published by Conti et al. (Conti et al. (2010)) the 3D geometry was based on a paradigm that accounted for the *in-vivo* geometrical asymmetry of the leaflets. The dimensions of the different parts of the model were based on measurements performed on cardiac magnetic resonance imaging (cMRI) on 10 healthy subjects, which were averaged over the to derive a representative model of the healthy AV. This models are still not fully representative of the anatomical variability which can be found in-vivo, and is therefore impossible to obtain subject-specific biomechanical information from these models. However, despite the limitations described above, the computed results confirmed that morphological differences between leaflet-sinus units induce important differences in stress values; thus, discarding a symmetrical design to adopt an asymmetrical one can provide more accurate stress-strain patterns. The third and current generation of geometrical models is based on the complete 3D reconstruction of patient-specific anatomies through the segmentation of clinical images such as CT, MRI, echocardiography (Labrosse et al. (2010), Chandran and Vigmostad (2013)). This models overcome the limitations described above and provide a more subject-related geometry. However, it has to be underlined that the final quality and accuracy of the model is strongly related to the image quality and resolution and to the image segmentation process. This models

represent the current state of the art.

The discretization of the domain is another important aspect of the modeling procedure, straightly following the AV geometry reconstruction. The output of the reconstruction process, in particular when dealing with subject-specific models, is a filtered point-cloud form which a set of 3D surface is defined (Sturla et al. (2016), Labrosse et al. (2010)). This surface has to be divided into a computational element grid in order to be suitable for numerical simulations. The element type and its characteristic dimension, i.e. the mesh size, are crucial aspects which entail the consistency and the reliability of the results obtained from the simulations. In the following, a brief introduction to different features impacting the discretization of the domain is presented.

Mesh size: the increasing of the mesh size is always related to a decreasing in computational costs, and this is an important aspect regarding the applicability of simulations. However, it may produce results with bad accuracy; hence, high mesh size produce big elements which generally are not able to correctly fit the represented geometry and also are not able to estimate the real variables pattern resulting in loss of essential information. To the best of our knowledge, in the field of domain discretization of the AV geometry, the vast majority of the published studies does not assume an element characteristic dimension higher than $1.0\,\mathrm{mm}$.

Element type: working on highly curved geometries, as the physiological anatomies AV cusps, generally makes it non-trivial to achieve a satisfactory mesh quality, i.e. to avoid excessively distorted elements that would be prone to generate artifacts in the subsequent simulations. This aspect contributes to driving the choice of the elements used in the discretization of the geometry, which may be linear or of higher order. Also, aortic valve leaflets may be discretized using solid, topologically 3D elements or shell elements, which are topologically 2D and assumed a plane stress state. Therefore, the element type choice has a critical impact on the whole numerical simulation procedure and the choice between shell elements and solid elements presents pros and cons on both side. However, a clear indication of which elements have to be used depending on the problem to tackle is still missing in the field of AV numerical simulations.

Finally it has to be noticed that, in addition to a complex, curved and subject-dependant leaflet shape, also the thickness of the AV leaflets is affected by anatomical variability between different subjects (Lacefield et al. (2004)). However, this information is not assessable from every clinical imaging technique: the average thickness of a physiological AV leaflet goes from 1.2 mm of the attachment edge to less than 0.4 mm of the belly re-

gion (Grande et al. (1998)), which is definitely lower than the maximum resolution of standard MRI exams, representing the most common imaging technique to assess cardiac function in pathological subject. However, from a modeling point of view it is reasonable to think that the impact of the leaflet thickness on the stress-strain behavior of the valve is not negligible; despite that, to the best of our knowledge, a clear investigation of this effect is missing.

In this scenario, we tested three working hypothesis related to the discretization of the computational domain and to the leaflets thickness distribution:

1. The use of solid elements in the discretization of leaflet geometry limits, or even prevents from, undesired and unrealistic local rotations of the leaflets at the insertion onto the aortic wall, thus leading to a more realistic configuration of the aortic valve when simulating its closure.

2. The use of solid elements in the discretization of leaflet geometry allows for capturing variations in strains and stresses through the thickness of the leaflets, which cannot be captured when using shell elements.

3. When using solid elements, different regional distributions of leaflet thickness may lead to markedly different results in terms of leaflet strains and stresses when simulating AR function throughout the cardiac cycle.

In order to test these hypothesis, we implemented a semi-automated tool for the generation of image-based aortic root FEMs; the tool allows for discretizing the valve leaflets using shell or solid hexahedral elements, and for setting space-dependent patterns of leaflets thickness for solid leaflets.

2.2 Definition of the modeling workflow

2.2.1 Acquisition of cMRI data, segmentation and model reconstruction

Our modelling approach was applied to the cMRI dataset of a 28 years old healthy volunteer, weighting 65 kg.

T1-weighted cine-cMRI sequences were acquired on 18 planes evenly rotated (one every $10°$) around the axis passing through the centre of the annulus and the centre of the sino-tubular junction (Figure 2.1.a). Acquisitions

were performed on a 1.5 T Achieva scanner (Philips Healthcare Medical System, Irvine, Calif). In-plane spatial resolution and slice thickness were equal to $1.10\,\mathrm{mm}$ and $7\,\mathrm{mm}$, respectively. 30 frames/cardiac cycle were acquired with R-wave triggering.

Images were manually processed in the first systolic frame, identified as the first frame characterized by an open aortic valve. As in previous studies (Conti et al. (2010), Soncini et al. (2009), Atkins et al. (2014)), the trans-valvular pressure acting on AV leaflets was considered negligible. In this configuration, processing was performed by in home Matlab$^\copyright$ software, which allows for tracing AR substructures by simply clicking multiple points on the image. In each plane, two annular points, which lay on the annulus, the Valsalva sinuses, two STJ points, and the ascending aorta were defined. Leaflets were traced only if clearly visible (Figure 2.1.b). Finally, when all AR substructures were traced, 20 to 25 points were selected. Tracing was performed by two independent observers, in order to asses the inter-observer variability of the procedure. Each traced profile is described by a cubic spline and sampled, so to export the in plane coordinates of a set of points for each traced structure.

These raw data are automatically transformed in the 3D space and filtered in order to eliminate the noise due to manual segmentation. A network of 3D splines is then generated on the aortic wall and on the leaflets, interpolating the filtered points (Figure 2.1.c). An optional smoothing operation was implemented in our script in order to assure a corner-free reconstruction of the leaflets surface; this procedure may be necessary when the leaflets are not clearly visible during the manual tracing. The 3D surface of the each AR structure is created on the profile of the splines and discretized with square shell elements; the entire procedure is handled by the CAD software Gambit$^\copyright$, which is fed with a text file (.*jou* format) where all of the operations are described. The input file is automatically generated by the Matlab$^\copyright$ tool. The mesh yielded by Gambit$^\copyright$ is further processed to connect the leaflets to the aortic wall, manipulating the connectivity matrix, and to generate the solid elements. A full volume mesh for the aortic wall was created using an extrusion procedure along the node normal (Figure 2.1.d); instead, depending on the model the user wants to generate, the mesh of the leaflet can be of three types:

- **SH** model: wall made of 8-node solid elements with reduced integration (Abaqus C3D8R elements); leaflets made of 4-node shell elements (Abaqus S4 elements, with only a virtual constant shell thickness).
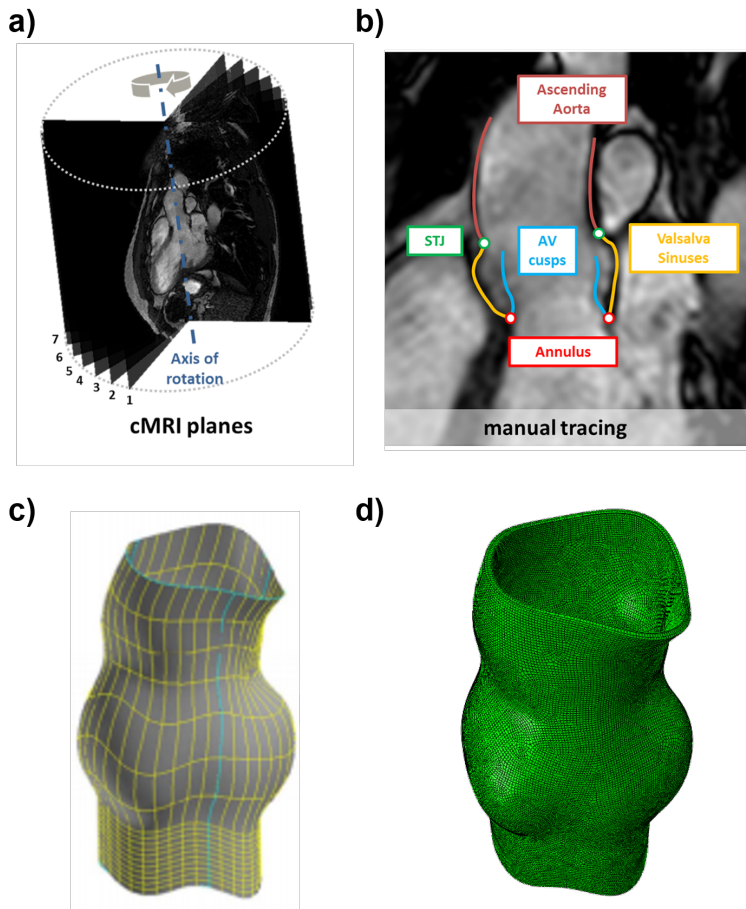
Figure 2.1: *cMRI data acquisition and image processing: a) cMRI cine protocol of acquisition; b) manual tracing of AR sub-structures on a cMRI plane including two annular points, the Valsalva sinuses, two STJ points, the ascending aorta, and leaflets whenever clearly visible; c) net Surfaces resulting from NURBS interpolation through bicubic surface; d) full solid mesh of the reconstructed model.*

- **3D-HT** (Homogeneous Thickness) model: wall made of C3D8R elements; leaflets made of three layers of 8-node solid elements (Abaqus C3D8 elements), obtained using a similar extrusion procedure to the one used for the wall elements but, in addition, a manipulation of the direction of the node normal was introduced in order to avoid mesh discrepancies.

- **3D-MT** (Modulated Thickness) model: wall made of C3D8R elements; leaflets made of three layers of 8-node solid elements (Abaqus C3D8 elements), obtained with the same procedure of 3D-HT model; in this case, a space-dependent thickness value for each point of the leaflet surface was assigned taking into account the physiological variations in aortic cusp thickness (Grande et al. (1998)).

2.2.2 Full volume mesh generation

In order to obtain a full volume mesh for both the aortic wall and the AV leaflets four main steps were implemented. Each step is described in the following:

Mesh continuity $\rightarrow$ This operation was performed for all models, and consisted of two manipulations. First, the nodes of the attachment-edge of each leaflet were ordered from the left to right looking the leaflet surface from the aortic side; the nodes of the corresponding sinus free-margin were ordered accordingly. Second, the node-to-node correspondence between sinus free-margin and leaflet attachment-edge was identified; since the two edges had approximately equal extent and were seeded with an equal number of nodes, the i-th node of one edge corresponded to the i-th node of the complementary edge. Based on this correspondence, mesh continuity could be easily imposed by manipulating the corresponding connectivity matrix, i.e. by substituting each node of the leaflet attachment-edge with the corresponding node of the sinus free-margin. The result was a new connectivity matrix in which elements of the leaflets and of the sinuses shared the same nodes at the interface (Figure 2.2). Preliminary tests showed that this procedure systematically yielded good quality meshes, provided that the characteristic dimension of the elements is lower than $1\,\mathrm{mm}$. However, this threshold corresponds to a rather coarse mesh in the context of AR finite element modeling.

Full volume mesh on the wall $\rightarrow$ This operation was performed for all models. For each 4-node element of the aortic wall surface, three layers of hexahedral solid elements with reduced integration (ABAQUS$^{\copyright}$ C3D8R elements) were generated. To this aim, an extrusion process was performed,
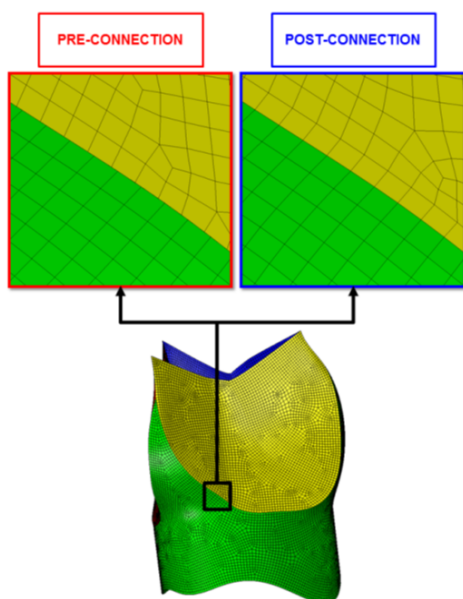
Figure 2.2: *Left hand panel: pre-connection procedure; leaflet side and the wall side do not share the same nodes. Right hand panel: post-connection procedure; elements of the leaflets and of the sinuses share the same nodes at the interface.*
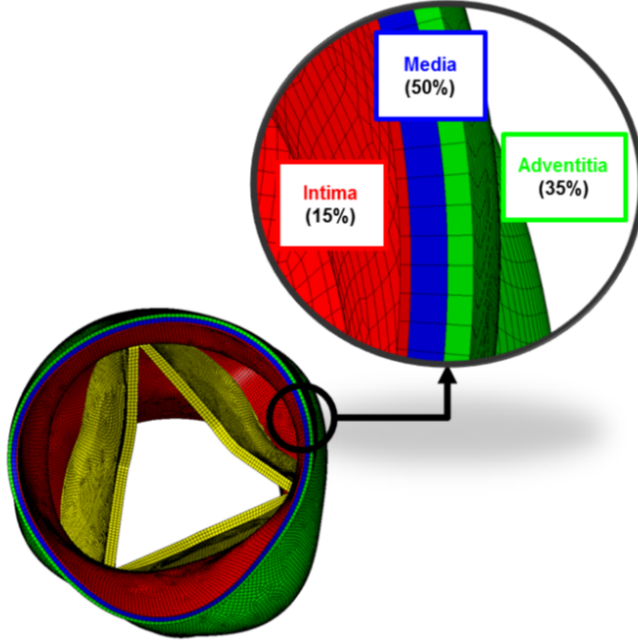
Figure 2.3: *Final AR solid mesh and percentage redistribution of the intima (15%), media (50%) and adventitia (35%) layer.*

where the original aortic wall nodes were copied and translated along the corresponding outward node normal. A wall thickness equal to $1.0\,\mathrm{mm}$ was set in each model. The three layers of solid elements through the wall thickness accounted for 15%, 50% and 35% of the total thickness, consistently with ratios between the thickness of the three wall tunicae reported in the literature (Grande et al. (1998)) (Figure 2.3). *Full volume mesh on the leaflets* $\rightarrow$ This operation was performed for 3D-HT and 3D-MT models only. An extrusion process similar to the one implemented to generate the solid mesh of the aortic wall was used for the creation of the AV leaflets solid geometry. Three layers of C3D8 elements were generated by copying and translating each node X_i of the leaflets along a specific vector v_i calculated as (Figure 2.4.a):

$$v_i = n_i(1 - e^{-\frac{C\alpha}{1-\alpha}}) + n_j(e^{-\frac{C\alpha}{1-\alpha}}) \tag{2.1}$$

where n_i is the local outward normal vector to the i-th node, n_j is the vector connecting X_j, the closest node to X_i on the sinus, and X'_j, the sinus closest node to X_j in the extrusion direction, α is the ratio between the euclidean distance d_{ij} and the maximum distance from the sinus side within the all
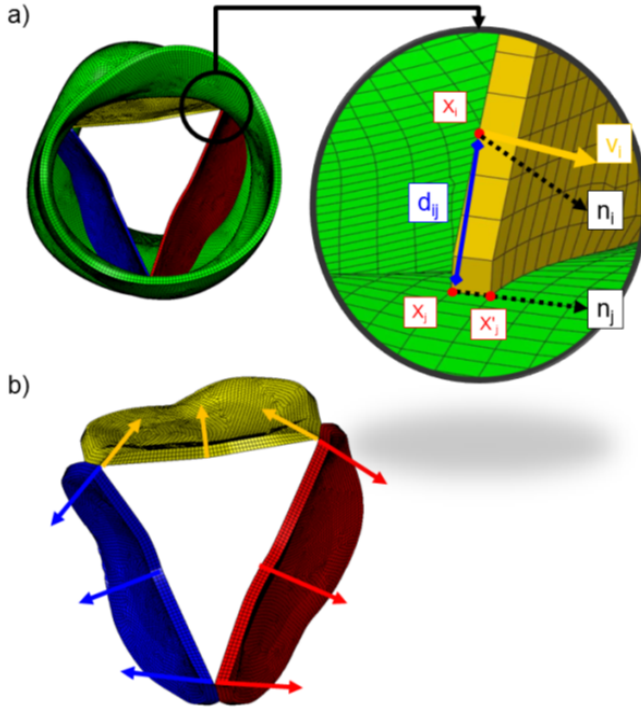
Figure 2.4: *Procedure to create a full volume mesh on the leaflets with an homogenous thickness value along the entire surface. a) An example of the normal vector manipulation performed on each node across the leaflet surface; the yellow vector, v_i, is the final vector along which the node X_i is extruded. b) The principal directions along which the extrusion process was performed are shown by the arrows.*

leaflets nodes, and C is a parameter that was empirically set equal to 2.5. In practise, the higher is the distance d_{ij}, the more v_i is a close approximation of n_i, the lower is the distance d_{ij}, the more v_i is a close approximation similar to n_j and aligned with the tangent to the aortic wall at the wall-leaflet interface. The final result are the three multi-layer leaflets shown in Figure 2.4.b.

Thickness modulation $\rightarrow$ This operation was performed for 3D-MT models only. During the creation of the leaflet volumetric mesh, for each node of the leaflet a space-dependent thickness value was assigned through an ad-hoc algorithm. Since the leaflet regional thickness was not assessable from cMRI, the thickness pattern was assumed based on region-dependent values reported in the literature and that were different for each leaflet (Fig-

ure 2.5) (Grande et al. (1998)). In order to reproduce the same variation in thickness, the original leaflet surface mesh were mapped; two euclidean distances were evaluated for each node: d_{FM}, the distance between the node and the corresponding closest node of the free-margin of the leaflet, and d_{AE}, the distance between the node and the corresponding closest node of the attachment-edge of the leaflet. The leaflet surface was divided in four regions according to the following rules:

1. $d_{FM} \leq 5\,\mathrm{mm} \wedge d_{AE} > 5\,\mathrm{mm} \rightarrow$ *free-margin region*: linear decreasing in thickness from $1.2\,\mathrm{mm}$ (mesh size) for the nodes closer to free-margin down to $0.3\,\mathrm{mm}$.

$$\Delta s = 1.2(1 - \alpha_{FM}) + 0.3\alpha_{FM} \quad \mathrm{mm}$$

where $\alpha_{FM} = d_{FM}/5$

2. $d_{AE} \leq 5\,\mathrm{mm} \wedge d_{FM} > 5\,\mathrm{mm} \rightarrow$ *attachment-edge region*: linear decreasing in thickness from $1.2\,\mathrm{mm}$ (mesh size) for the nodes closer to attachement-edge down to $0.3\,\mathrm{mm}$.

$$\Delta s = 1.2(1 - \alpha_{AE}) + 0.3\alpha_{AE} \quad \mathrm{mm}$$

where $\alpha_{AE} = d_{AE}/5$

3. $d_{FM} > 5\,\mathrm{mm} \wedge d_{AE} > 5\,\mathrm{mm} \rightarrow$ *belly region*: constant thickness equals to $0.3\,\mathrm{mm}$.
$$\Delta s = 0.3 \quad \mathrm{mm}$$

4. $d_{FM} \leq 5\,\mathrm{mm} \wedge d_{AE} \leq 5\,\mathrm{mm} \rightarrow$ *intersection region*: decreasing in thickness from $1.2\,\mathrm{mm}$ (mesh size) for the nodes closer to attachement-edge down to $0.3\,\mathrm{mm}$.

$$\Delta s = 2 \times 0.3 \frac{5+5}{d_{FM} + d_{AE}} \quad \mathrm{mm}$$

In the case of nodes with d_{FM} and d_{AE} both equal to zero a control was implemented to set $\Delta s = 1.2\,\mathrm{mm}$. Moreover, for small values of d_{FM} and d_{AE} the value of Δs could be greater than $1.2\,\mathrm{mm}$: in that case another control set this parameter equal to $1.2\,\mathrm{mm}$.

At the end of the procedure a volumetric mesh with three layers was created for each leaflet; at each point of the leaflet surface, the thickness of each layer was exactly one third of the total thickness value. The described procedures allowed to obtain the final 3D discretized geometrical model

29
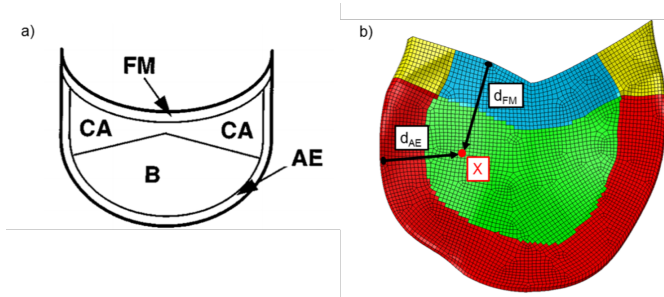
Figure 2.5: *Thickness modulation procedure: a) diagram of leaflet regions. B: belly, FM: free margin, CA: coaptation area, AE: attachment edge. b) the four regions created in our model for the thickness modulation: blue: free-margin region; red: attachment-edge region yellow: intersection region; green: belly region. X is a generic point inside the leaflet surface, d_{FM} and d_{AE} era the corresponding distances from the two boundary edges (Free Margin, d_{FM}; Attachment Edge, d_{AE}) used to map the nodes across the leaflet surface. In this case, these two distances are higher than the corresponding thresholds, hence the point belongs to the belly region and a thickness value of $0.1\,\mathrm{mm}$ was assigned to it.*
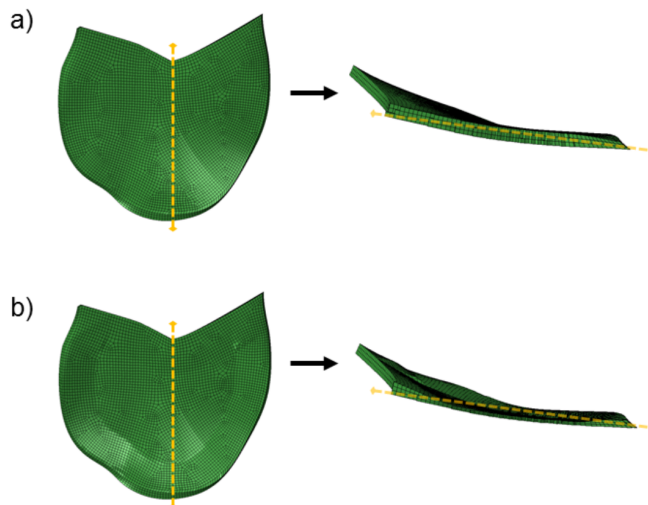
Figure 2.6: *Differences between a leaflet with and without a modulated thickness: a) frontal view (left hand panel) and a section (right hand panel) of the leaflet with a constant thickness. b) frontal view (left hand panel) and a section (right hand panel) of the leaflet with a modulated thickness.*

of the AR. The corresponding definition, together with the definition of the tissues mechanical properties and of the boundary conditions (see sections 2.2.3 and 2.2.4), was automatically written in the input (*.inp*) files for the subsequent simulations in ABAQUS/Explicit.

2.2.3 Tissues mechanical properties

Two different material formulations were used in our AR model, one for the aortic wall and another one for the valve leaflets. The mechanical response of the aortic wall was assumed linear, elastic and isotropic, with a $2\,\mathrm{MPa}$ Young's modulus and a 0.45 Poisson's ratio to reproduce the almost incompressible behavior of the real tissue (Conti et al. (2010)). AV leaflets tissue was described as a transversely anisotropic and hyperelastic material through the model originally proposed by Guccione and colleagues (Guccione et al. (1991)) to mimic the passive response of myocardial tissue. This model is based on the following strain energy function U:

$$U = \frac{C}{2}(\exp Q - 1) + K(\frac{J^2 - 1}{2} - \ln J) \tag{2.2}$$

where C is the first constitutive parameter in MPa, J the $detF$, K the compressibility module and Q is formulated as follow:

$$\begin{aligned} Q = {}& 2b_1 tr(E) + b_2 E_{ff}^2 + \\ & + b_3(E_{ss}^2 + E_{nn}^2 + E_{sn}^2 + E_{ns}^2) + \\ & + b_4(E_{nf}^2 + E_{fn}^2 + E_{fs}^2 + E_{sf}^2) \end{aligned} \tag{2.3}$$

The terms E_{ij} are the components of the Green-Lagrange strain tensor, expressed with reference to a coordinate system f, s, n whose axes are aligned with preferentially oriented fibers (f) and orthogonally to them (n, s). In the model, f, s, n were considered aligned with the commissure-commissure, annulus-to-free margin and through-thickness direction, respectively. b_1, b_2, b_3 and b_4 are the other constitutive parameters; so the model just needs six parameters (C, b_1, b_2, b_3, b_4, K) to completely describe the material properties. These were identified based on experimental data from biaxial tensile tests by Stella and Sacks (2007). The parameter set that we obtained assured a very good fitting (Figure 2.7), with an average mean quadratic error $err = 5.4 \cdot 10^{-5}\mathrm{MPa}$, for maximum stresses in the order of $5 \cdot 10^{-1}\mathrm{MPa}$. The values found were equal to: $C = 1.41 \cdot 10^{-4}\mathrm{MPa}, b_1 = 0.0, b_2 = 22.7785, b_3 = 3.4995, b_4 = 9.9630$.
The constitutive model was implemented into a VUANISOHYPER_STRAIN
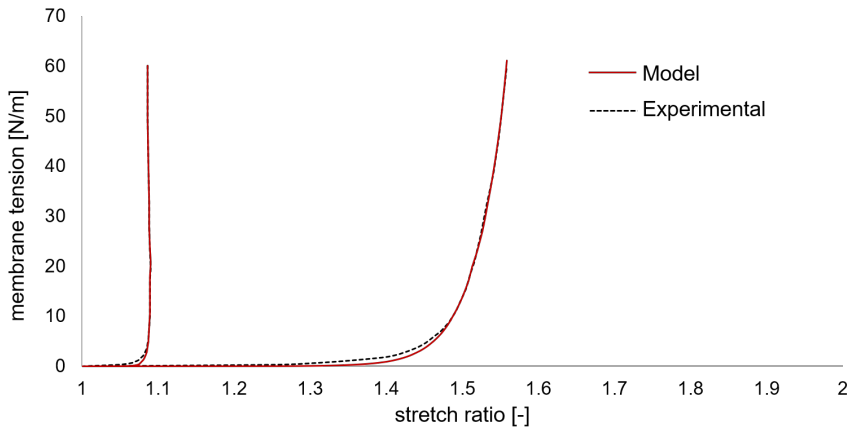
Figure 2.7: *Fitting (solid line) of the experimental data from Stella and Sacks (2007) (dashed line). On the left the circumferential direction curve, on the right the radial direction curve.*

subroutine for ABAQUS/Explicit$^{©}$.

A density equal to $11\,\mathrm{g/cm^3}$, 10-fold the physiological value, was assumed for all AR's tissue taking into account the inertia related to the presence of the blood.

2.2.4   Computation of AR biomechanics

The initial configuration of the AR was defined at early systole, when AV leaflets are approximately unloaded. Hence, cMRI data in the first systolic frame were used to define AR reference geometry. The finite element computation of the pre-stress field acting on the AR in this configuration was required. To this aim, an iterative process was performed as described in detail in a recent work (Votta et al. (2017)); briefly: the stress-free AR configuration was pressurized by applying a pressure load of $82\,\mathrm{mmHg}$ to the inner surface of the aorta and of the aorto-ventricular junction; then, the computed nodal displacement field was checked for the entire aortic wall; if the peak value of displacement magnitude did not exceed the in-plane resolution of cMRI, that inflated configuration was considered equivalent to real configuration related to the cMRI, and the corresponding Cauchy true stress field characterizing the aortic wall was considered the pre-stresses field to be applied when simulating AR biomechanics throughout the cardiac cycle (Figure 2.8). Otherwise, the stress-free AR configuration was updated and set equal to inflated configuration just obtained, and the pres-
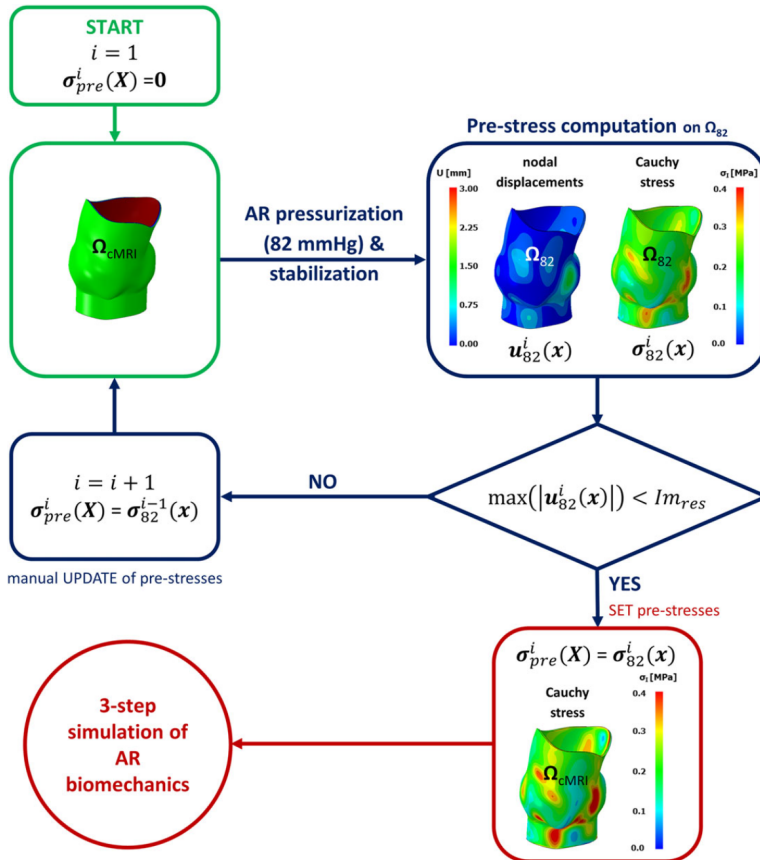
Figure 2.8: *Workflow of the iterative prestress computation developed in the work of Votta et al. (2017).*

surization simulation was performed again.

After that, the structural response of the pre-stressed AR over two consecutive cardiac cycles was computed; to this aim, physiological time-dependent ventricular and aortic pressures were applied to relevant regions of the aortic wall and a consistent trans-aortic pressure drop to the leaflets' surfaces.

2.3   Results

The final geometry of the three models generated is shown in Figures 2.9.
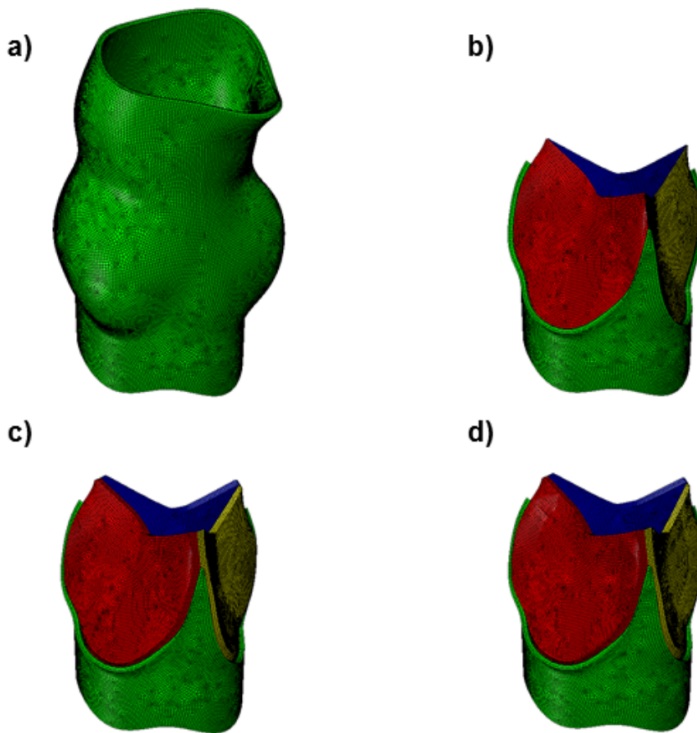
Figure 2.9: *Geometry reconstruction starting from cMRI. a) aortic root wall (equal for all models). b) leaflets' structure in the model SH. c) leaflets' structure in the model 3D-HT. d) leaflets' structure in the model 3D-MT.*

As described in the previous chapter, for each model typology (SH, 3D-HT, 3D-MT) a simulation sequence was performed, which consisted in the iterative computation of aortic wall pre-stresses and in the subsequent simulation of the structural response of the pre-stressed AR throughout two

| | 1a | 1b | 2a | 2b | 2c |
	P-S [h]	OP [min]	INIT [h]	CC #1 [h]	CC #2 [h]
SH	6.5	~15	6.9	14	13.5
3D-HT	6	~15	6.1	13	12
3D-MT	6	~15	6.1	13	12

Table 2.1: *Time required by the different phases of our simulation process. The computation of AR pre-stresses required two iterations of phases 1a and 1b. P-S = pre-stress evaluation step. OP = operator-dependent step. INIT: initial phase in which the pre-stressed AR configuration is reached. CC = cardiac cycle step.*

consecutive cardiac cycles, starting from the first systolic frame yielded by cMRI.

Table 2.1 summarizes the time required by the different phases of our simulation process; the time-expense of simulations is referred to a workstation with 16 CPUs. It is worth noting that the output of the pre-stress computation (phase 1a) are manually integrated into the input file for the simulation of the cardiac cycles (phases 2a-b-c); this manual operation requires approximately 15 minutes. As already mentioned, pre-stress computation was an iterative process which in our case required two iterations. Results were post-processed with reference to the second simulated cardiac cycle, in order to account for the transient condition characterizing the initial time-point of the phenomenon and for the associated inertial effects (Conti et al. (2010)). For each quantity of interest, results from SH model and 3D-HT model were compared in order to quantify the effects of the use of solid elements in the discretization of leaflet geometry. Also, results from 3D-HT model and 3D-MT model were compared to assess the effects of different leaflet thickness distributions.

2.3.1 Aortic valve time-dependent configuration

AV configuration was assessed at two key time-points through the cardiac cycle: at peak systolic trans-valvular pressure ($t = 20\,\text{ms}$), and at peak diastolic-transvalvular pressure ($t = 380\,\text{ms}$).

At peak systole, the leaflet configuration was quantified in terms of orifice area (OA) (Figure 2.10). The OA of the 3D-HT and 3D-MT models showed a smaller orifice areas, by 13% and 16% respectively, as compared
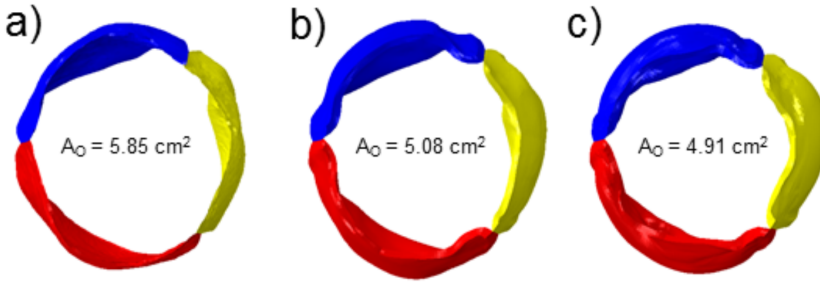
Figure 2.10: *Opened AV configuration and the corresponding orifice area (A_O) at the systolic peak ($t = 20$ ms). a) SH models. b) 3D-HT models. c) 3D-MT models.*

	SH model			3D-HT model			3D-MT model		
	LC	RC	NC	LC	RC	NC	LC	RC	NC
Coaptation height [mm]	19.81	17.85	17.58	19.69	18.40	18.53	20.21	17.66	17.95
Prolapse [mm]	1.67	3.77	1.51	0.50	1.65	1.35	0.66	2.07	2.11

Table 2.2: *Coaptation height and degree of prolapse values computed for all models at peak diastole.*

to the SH model. This result is likely due to the different behavior of the leaflets at their line of insertion. When shell elements were used to discretize leaflets' geometry, the leaflet-aortic wall connection behaved approximately as a spherical joint, and leaflets were allowed for local wide rotations (Figure 2.11 , *left hand panel*). When solid elements were used to discretize leaflets geometry, the leaflet-aortic wall connection behaved as a deformable encastre, preventing from free rotations of the leaflet section (Figure 2.11 , *right hand panel*). This effect reflected into a less pronounced outward motion of the leaflet during the opening phase. At peak diastole, leaflet configuration was analyzed qualitatively (Figure 2.11) and quantitatively by measuring the coaptation height and the degree of prolapse of the leaflets. The former was defined as the axial distance in mm between the nodulus of Arantius and the annular plane. The latter was defined as the distance in mm, oriented towards the ventricle, between the lower point in the leaflet and the corresponding nadir (Table 2.2). As regards the coaptation height, no systematic differences were observed between models using different types of element to discretize the leaflets geometry. The main evidence was that in all models coaptation height values were higher than the
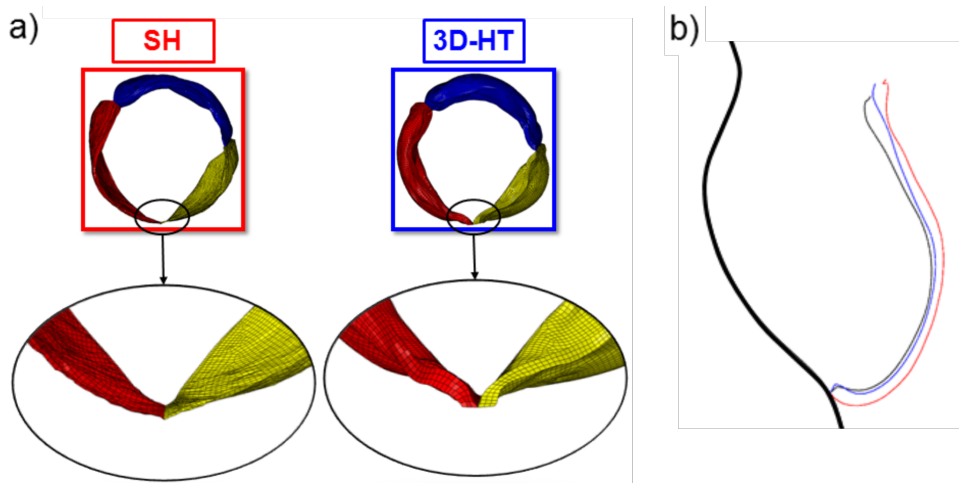
Figure 2.11: *Panel A: the different deformed configuration of the commissural region of the leaflets at peak systole when using shell elements (left panel) and solid elements with homogeneous thickness (right panel) to discretize the leaflets is depicted for model AR1. In particular, the junction between the aortic wall, the left-coronary leaflet (LC, yellow), and the right-coronary leaflet (RC, red) is reported. Panel B: longitudinal section of the left-coronary leaflet at the diastolic peak ($t = 380\,\mathrm{ms}$). Black line: sinus side and the LC leaflet of the model 3D-MT with a modulated thickness. Blue line: the LC leaflet of the model 3D-HT with an homogeneous thickness. Red line: the LC leaflet of the model SH with an homogeneous virtual thickness.*

ones provided by previously published computational studies Conti et al. (2010) and were all well above the $9\,\mathrm{mm}$ upper threshold characterizing almost all patients suffering from moderate or severe aortic insufficiency according to ultrasound analyses Bierbach et al. (2010). Of note, the high values of the coaptation height parameter may have been influenced by the smoothing procedure adopted in the 3D reconstruction of leaflets geometry. Indeed, that procedure was aimed also at avoid unrealistically steep profiles of the leaflet free margin and, to this specific aim, slightly elevates the central portion of the free margin.

As regards the degree of prolapse, a notable difference was observed between the models using different elements to discretize the leaflets geometry. In general, SH models were characterized by a more pronounced degree of prolapse, i.e. the belly region of the leaflets tended to invade the volume within the aorto-ventricular junction. Again, this effect was likely due to the connection between the leaflet mesh and the aortic wall mesh, where nodes were allowed for finite rotations. This effect was markedly reduced in the 3D-MT and in the 3D-HT models, owing to the connection between leaflet and aortic wall meshes, which in these models acts like a deformable encastre (Figure 2.11).

2.3.2 Mechanical response of the aortic valve

The mechanical response of the AV during the cardiac cycle was evaluated through the analysis of the stress-strain state. In particular, we focused the attention on the stress and strain patterns of the belly throughout the cardiac cycle, due to the fact that it is the most stressed region of the cusp, as reported from literature (Conti et al. (2010), Grande et al. (1998), Chandran and Vigmostad (2013)). To this aim, a $4\,\mathrm{mm} \times 4\,\mathrm{mm}$ patch in the central portion of the belly was considered; stress and strain values were assessed for all elements within the patch, and their values were averaged over the patch (Figure 2.12). The first important result was the difference between the two characteristic directions of the models, circumferential and radial, highlighting the anisotropy of the aortic valve tissue. During the closing valve transient, the deformations of the cusps rapidly increase to reach a plateau during the diastole phase. Despite the magnitude, this behavior could be observed in all models, coherently with the data reported in the work of Thubrikar (M. Thubrikar (1979)). In addition, while in the radial direction the deformation magnitudes were consistent with literature (M. Thubrikar (1979), Conti et al. (2010)), the ones in circumferential direction overestimated the *in vivo* values. Regarding the stress patterns, we
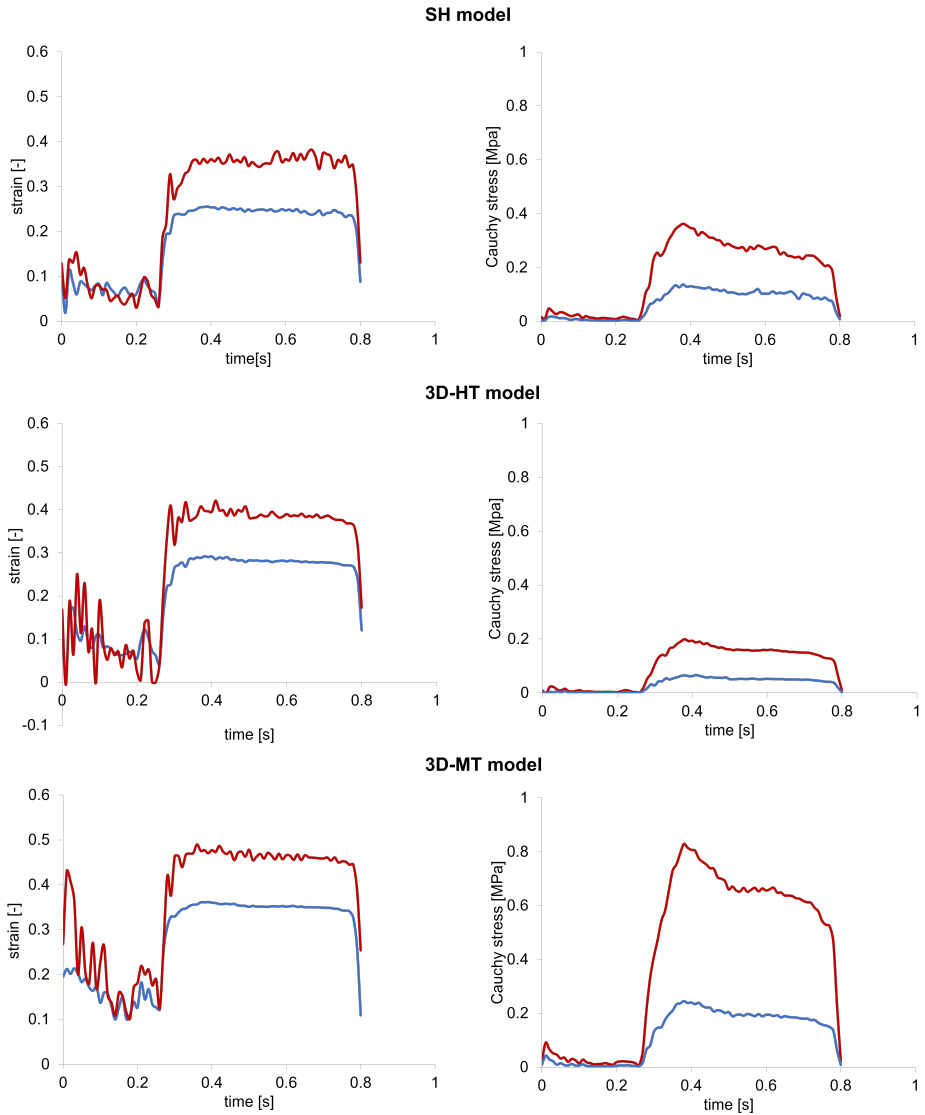
Figure 2.12: *Left hand panel: nominal strain in the belly region throughout the entire cardiac cycle. Right hand panel: Cauchy stress in the belly region throughout the entire cardiac cycle. The blue lines represent the circumferential direction and the red ones the radial direction.*

could see a rapid increase during the closing valve transient, with the stress maximum values at the diastolic peak. For the same reasons causing the high degree of prolapse, i.e. the thinned belly region, the stress in the 3D-MT model showed very high values compared to the SH and 3D-HT models.

In order to deeply investigate the mechanical response of the aortic valve, we focused our attention on the diastolic peak ($t = 380\,\text{ms}$), because it represents the moment within the cardiac cycle in which the belly region is more stressed (Conti et al. (2010)). In particular, two kind of results were analyzed: the max principal, circumferential and radial stress, and the max principal stress and strain distribution along the leaflet surface viewed from the ventricular side. The differences in the element formulation between shell and solid models were evident (Figure 2.13): in shell leaflets the stress and strain patterns showed a patchy distribution, and a clear separation between the belly region and the coaptation area based on this pattern could not be detected. Conversely, in the solid 3D-HT and 3D-MT models the distribution was much more regular and a clear separation between these two regions was evident.

Calculated stress values (Table 2.3) proved the strong impact of the thick-
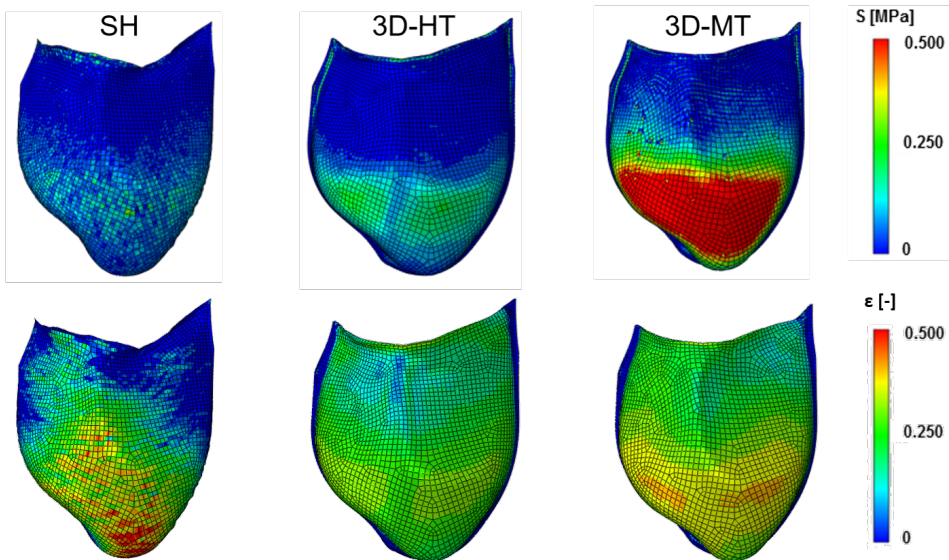
Figure 2.13: *Max principal stress (first line) and strain (second line) computed at the diastolic peak ($t = 380\,\text{ms}$). Right figure: mid surface of the SH model. Central figure: mid solid level of the 3D-HT model. Right figure: mid solid level of the 3D-MT model.*
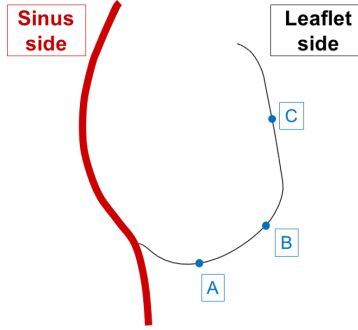
Figure 2.14: *Schematic longitudinal section representing the locations (green points) across the leaflet surface in which the max principal stress was evaluated.*

ness modulation procedure on the 3D-MT model; in particular, max principal, radial and circumferential stresses were notably increased in the thinned belly region. For example, the circumferential stress values averaged over the three leaflets for the 3D-MT model are more than 4-fold as compared to the corresponding values for 3D-HT model, and more than 2-fold as compared to the corresponding values for SH model. As one of the primary

	SH model			3D-HT model			3D-MT model		
	LC	RC	NC	LC	RC	NC	LC	RC	NC
Max principal stress [MPa]	0.338	0.566	0.317	0.163	0.254	0.196	0.681	1.028	0.861
σ_{circ} [MPa]	0.312	0.489	0.287	0.156	0.249	0.192	0.636	1.008	0.842
σ_{rad} [MPa]	0.088	0.220	0.103	0.037	0.102	0.056	0.136	0.375	0.225

Table 2.3: *Max principal stress, circumferential stress (σ_{circ}) and radial stress (σ_{rad}) for the three leaflets (LC, RC, NC) of each model at diastolic peak ($t = 380\,\text{ms}$).*

aims of this work was the investigation of the stress distribution across the leaflet thickenss, the circumferential and radial stress were evaluated across the leaflet surface in all models. The measures were performed at the diastolic peak ($t = 380\,\text{ms}$) in three different points (A, B, C) of the left-coronary leaflet (Figure 2.14). In this analysis a particular aspect has to be accounted in regarding how the stress values are computed through the leaflet thickness. For each location the stress value were available in three integration point across the leaflet thickness for all models: for the SH models this three points refer to three shell layers (virtual ventricular layer, mid

Location		σ_{circ}			σ_{rad}		
		SH	3D-HT	3D-MT	SH	3D-HT	3D-MT
	V layer	0.252	0.144	0.315	0.133	0.074	0.149
A	mid layer	0.045	0.066	0.241	0.026	0.040	0.117
	A layer	0.109	0.029	0.183	0.140	0.021	0.090
	V layer	0.526	0.229	0.770	0.115	0.063	0.232
B	mid layer	0.096	0.170	0.640	0.025	0.050	0.198
	A layer	0.169	0.135	0.548	0.127	0.037	0.170
	V layer	0.022	0.009	0.051	0.005	0.001	0.023
C	mid layer	0.016	0.021	0.071	0.005	0.002	0.029
	A layer	0.038	0.046	0.106	0.035	0.010	0.036

**Table 2.4:** *Circumferential stress and radial stress within the cross section of the LC leaflet at diastolic peak (t = 380 ms). V side = ventricular layer of the leaflet surface. mid plane = middle layer of the leaflet surface. A side = aortic layer of the leaflet surface.*

layer, virtual aortic layer), while for the 3D-HT and 3D-MT models the integration points lay in three different solid elements layers (solid ventricular layer, solid mid layer, solid aortic layer). Due to the different formulation between shell and solid elements, the stress values at the integration points are computed in a completely different way, leading to different levels of precision (Table 2.4). The most evident stress gradient through the leaflet thickness was obtained at location A and B, consistently with the marked local curvature. Of note, in SH models the V side and the A side exhibited an even more patchy and noisy stress distribution as compared to the mid section (Figure 2.15); hence, side-to-side stress variations are not reliable in these models, and only results for 3D-HT and 3D-MT models can be considered reliable.

2.4 Discussion

The principal novelty of this work is the development of an automated tool allowing for i) creating subject-specific, image-based AR geometrical models capturing the anatomical details, ii) discretizing the reconstructed geometry obtaining a high quality mesh of hexahedral elements, iii) defining a space-dependent pattern of leaflet thickness, which can be tuned based on
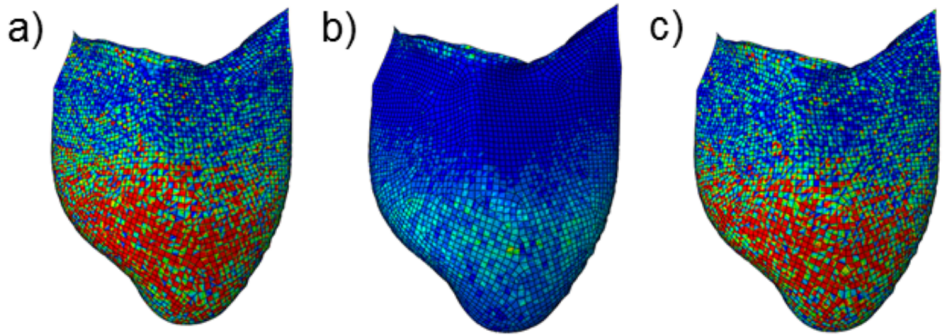
Figure 2.15: *Stress distribution on the V side (a), mid-section (b) and A side (c) for the SH model of the LC leaflet.*

patient-specific data or on data from the literature, and iv) preparing the input files required to simulate the structural response of the pre-stressed throughout the cardiac cycle. To the best of our knowledge, no previous work published in the literature combines these features.

Among these features, the second and third ones proved particularly relevant when computing aortic valve biomechanics, and in particular when assessing peak diastolic stresses. On one hand, we compared their distribution computed when aortic valve leaflets were discretized into uniformly thick hexahedral elements and into uniformly thick shell elements, respectively. In the former case, the computed stress distribution was much more regular and consistent with the function fulfilled by the different leaflet regions. This first result strongly suggests that the use of hexahedral elements represents an advancement as compared to the more common use of shell elements. Moreover, when hexahedral elements were used the stress gradient through the leaflet thickness could be reliably computed, whereas this computation was not reliable when using shell elements. This second result has implications regarding a possible application of this type of models, i.e. the analysis of the different strain and stress levels characterizing the three aortic leaflet layers, which could be relevant to the better understanding of pathological processes such us the progression of calcific aortic valve disease.

On the other hand, we also compared the stress distribution computed when discretizing the valve leaflets into hexahedral elements with uniform and space-dependent thickness, respectively. In the latter case, the entity of computed stresses changed notably; in particular, stresses experienced by the belly region, which was thinner when setting a space-dependent thick-

ness distribution from the literature (Conti et al. (2010)), were increased by up to 5-fold. This result highlights that, as expected, changes in leaflet thickness have a major impact of leaflet stresses. In the context of subject-specific AR structural modeling, the implication of this third result is that it should be mandatory to exploit image modalities that, differently from cMRI, allow for quantifying the subject-specific regional thickness of aortic valve leaflets, in that this is a key feature when quantifying aortic valve structural response. In this regard, 3D ultrasound imaging may represent a valuable option. Alternatively, age- and gender-matched, as well as class-matched (e.g. healthy valve, calcific valve, Marfan syndrome-affected valve) thickness patterns should be identified based on *ex vivo* measurements on cadavers or on tissue samples resected during surgical procedures.

Despite being an advancement of the state of the art, the modeling approach herein proposed could be further improved.

As far as geometrical reconstruction is concerned, the most important improvement should regard the generation of the solid model of the aortic wall. With the current procedure wall thickness cannot be set to any reasonable value; if wall regions with a marked concavity towards their outward surface are present, in these regions the generation of hexahedral elements works only if relatively small values ($\leq 1\,\mathrm{mm}$) are assigned to the wall thickness. Otherwise, "twisted" elements are generated. In order to overcome this limitation, the extrusion process implemented to generate the hexahedral elements should be modified. Alternatively, extra functions should be added to the developed script to correct *ex post* the twisted elements, for instance by manipulating the connectivity of the generated solid mesh.

As far as the modeling of tissues' mechanical properties is concerned, two improvements should be implemented in the future. The first one regards the modeling of aortic wall mechanical properties and would consist in moving from a linear, elastic and isotropic constitutive model to a hyperelastic and anisotropic model. Of note, this improvement would imply a major complication in the computation of AR pre-stresses in the initial geometrical configuration reconstructed from medical images. Currently, the computation of pre-stresses exploits the *INITIAL CONDITION keyword available in the commercial solver used to perform the finite element simulations, i.e. ABAQUS/Explicit. However, this keyword is not compatible with the use of hyperelastic and anisotropic materials, and its exploitation become not trivial when simply a non-linear stress-strain behavior is assumed. As a result, a different method should adopted to compute pre-stresses. The same issue is present in case we would like to include

pre-stresses also in the leaflets themselves; in this work these pre-stresses have been neglected, starting from the consideration that the early systolic configuration is known to be "stress-free", but this aspect might have a relevant impact and should be better investigated in the future. The second improvement regards the modeling of aortic valve stress-strain response, and in particular the structural distribution of the collagen fibers within the leaflet surface, e.g. starting from experimental data on excised leaflets. This development would allow for moving towards a more precise prediction of the leaflets structural response and could pave the way towards a more precise study of tissue remodeling and degenerative process, such as for example the calcific aortic valve.

Bibliography

Atkins, S. K., Cao, K., Rajamannan, N. M., and Sucosky, P. (2014). Bicuspid aortic valve hemodynamics induces abnormal medial remodeling in the convexity of porcine ascending aortas. *Biomechanics and Modeling in Mechanobiology*, 13(6):1209–1225.

Bierbach, B. O., Aicher, D., Issa, O. A., Bomberg, H., Gräber, S., Glombitza, P., and Schäfers, H.-J. (2010). Aortic root and cusp configuration determine aortic valve functionâ. *European Journal of Cardio-Thoracic Surgery*, 38(4):400–406.

Chandran, K. B. and Vigmostad, S. C. (2013). Patient-specific bicuspid valve dynamics: Overview of methods and challenges. *Journal of Biomechanics*, 46(2):208–216.

Conti, C. A., Votta, E., Della Corte, A., Del Viscovo, L., Bancone, C., Cotrufo, M., and Redaelli, A. (2010). Dynamic finite element analysis of the aortic root from MRI-derived parameters. *Medical Engineering and Physics*, 32(2):212–221.

Gnyaneshwar, R. and Kumar, R. K. (2002). Original article : cardiovascular Dynamic analysis of the aortic valve using a finite. 73(4):3–6.

Grande, K. J., Cochran, R. P., Reinhall, P. G., and Kunzelma, K. S. (1998). Stress variations in the human aortic root and valve: The role of anatomic asymmetry. *Annals of Biomedical Engineering*, 26(4):534–545.

Guccione, J. M., McCulloch, A. D., and Waldman, L. K. (1991). Passive material properties of intact ventricular myocardium determined from a cylindrical model. *Journal of biomechanical engineering*, 113(1):42–55.

Labrosse, M. R., Lobo, K., and Beller, C. J. (2010). Structural analysis of the natural aortic valve in dynamics: From unpressurized to physiologically loaded. *Journal of Biomechanics*, 43(10):1916–1922.

Lacefield, J. C., Weaver, J., Spence, J. R., Dunmore-Buyze, J., and Boughner, D. R. (2004). Three-dimensional visualization and thickness estimation of aortic valve cusps using high-frequency ultrasound. *Physiological Measurement*, 25(1):27–36.

M. Thubrikar, W. C. Piepgrass, T. W. S. S. P. N. (1979). *Surgical Forum*, (30):241–243.

Soncini, M., Votta, E., Zinicchino, S., Burrone, V., Mangini, A., Lemma, M., Antona, C., and Redaelli, A. (2009). Aortic root performance after valve sparing procedure: A comparative finite element analysis. *Medical Engineering and Physics*, 31(2):234–243.

Stella, J. A. and Sacks, M. S. (2007). On the Biaxial Mechanical Properties of the Layers of the Aortic Valve Leaflet. *Journal of Biomechanical Engineering*, 129(5):757.

Sturla, F., Ronzoni, M., Vitali, M., Dimasi, A., Vismara, R., Preston-Maher, G., Burriesci, G., Votta, E., and Redaelli, A. (2016). Impact of different aortic valve calcification patterns on the outcome of transcatheter aortic valve implantation: A finite element study. *Journal of Biomechanics*, 49(12):2520–2530.

Votta, E., Presicce, M., Della Corte, A., Dellegrottaglie, S., Bancone, C., Sturla, F., and Redaelli, A. (2017). A novel approach to the quantification of aortic root in vivo structural mechanics. *International Journal for Numerical Methods in Biomedical Engineering*, 33(9):1–22.

Chapter 3

Subject-specific multiscale modeling of aortic valve biomechanics

This chapter was based on:

3.1 Introduction

The aortic root (AR) is the bulb-like functional and anatomical unit connecting the outlet of left ventricle to the ascending aorta. The aortic valve (AV) is the central structure in the AR; it is normally composed of three leaflets that, in physiologic conditions, open when the left ventricle contracts (systole) ejecting blood into the aorta. The leaflets are characterized by a three-layered structure: the fibrosa layer, made of circumferentially oriented collagen fibers of type I, faces toward the aorta; the spongiosa layer composed of proteoglycans (PGs)/glycosaminoglycans (GAGs) and the ventricularis layer, mainly composed of radially oriented elastin fibers, faces toward the left ventricle (Brazile et al. (2015)). During the cardiac cycle, the AV is normally subject to rapid and continuous pressure changes. These not only are responsible for the cycling opening and closure of the valve, but they are also transmitted to the tissue layered structure and finally down to the cell scale where they are known to regulate the matrix-maintaining role of the cusps valve interstitial cells (VICs) (Taylor et al. (2003)). Variations in the physiological macroscopic mechanical stimuli may alter this matrix-maintaining role, leading to pathological tissue remodeling, as in calcific AV (Otto (2002)); for this pathology the fibrosa layer of the AV leaflets plays a key role, being the place where the formation and growth of calcific noduli take place (Aikawa and Libby (2017)). This evidence suggests for the fibrosa a leading role in AV remodeling processes, despite the presence of VICs in both the fibrosa and ventricularis layers, suggesting the need for the investigation of the stress-strain distribution within the leaflet thickness during the cardiac cycle. As the understanding of remodeling driven pathology is of strong clinical interest, not only for the AV but also for the other heart valves, research investigating the mechanism of stimuli transmission from the organ to the cell scale has grown significantly in the recent past (Lee et al. (2015), Merryman et al. (2005), Rutkovskiy et al. (2017)). In this context FE simulations have been largely used for the simulation of AV behavior at different scale. However, despite the simulation of the AV biomechanical behavior at different scales has been deeply investigated separately, to the best of our knowledge few works tackled the multiscale relationship among the different scales of the AV using FE numerical simulations (Weinberg and Mofrad (2007), Weinberg et al. (2010)).

The organ scale biomechanics has been widely investigated in the last decades and the quantitative reconstruction of AV geometry is the first step towards the implementation of a structural model. In terms of geometrical realism,

two main classes of models can be identified in the literature: first, models relying on a very simple and idealized geometry (Gnyaneshwar and Kumar (2002)) an second, models based on the 3D reconstruction of subject-specific anatomies through the segmentation of clinical images (Labrosse et al. (2010), Auricchio et al. (2014), Votta et al. (2017)). These models represent the current state of the art and are the only way to get simulation output from real anatomical data. The second important step is a cross challenge between the different length scale: modeling the mechanical behavior of different AV tissues which are anisotropic and non-linear. Several experimental tests have been conducted on intact AV leaflets (Billiar and Sacks (2000)) and on the different tissue layers (Stella and Sacks (2007), Sacks and Yoganathan (2007)) to estimate the stress-strain behavior, and this data have been later represented using different constitutive models in FE simulations (Conti et al. (2010), Kim et al. (2007)). Cell mechanical behavior is still a challenge as we do not have direct measurements of the VICs mechanical properties; at this scale only micropipet aspiration estimation of elastic modulus of VICs are available (Merryman et al. (2005)). Understanding the role of biomechanics in the complex remodeling pathways will be greatly enhanced by a framework for relating AV macroscopic strains and stresses to the mechanical stimuli experienced by VICs. The state of the art work in this context is the one published by Weinberg and Mofrad (2007). This work used a fully three-dimensional AV geometry, including appropriate nonlinear, anisotropic material models; the organ-scale model is a dynamic fluid-structure interaction that predicts the full cycle of opening and closing, the tissue-scale model simulates the behavior of the AV cusp tissue multiple layers, while the cell-scale model predicts cellular deformations of individual cells within the cusps. Despite this work represent a solid multiscale approach, two main limitation are still present: firstly the organ scale anatomy is paradigmatic, preventing form considerations related to the subject-specific anatomical features of the model, and secondly all simulations are linked by displacement boundary conditions. With the aim of improving these two modeling aspects, in the present work we propose a more exhaustive finite element (FE) multiscale model allowing for the computation of cardiac cycle AV biomechanics at the organ length-scale accounting for the subject-specific anatomy, and able to scale the obtain information down to the cell length-scale. To this purpose displacement boundary conditions were used to transfer the data from the organ to the tissue length scale, while stress boundary conditions were used to pass from the tissue to the cell scale. The workflow was applied to three subject-specific AV anatomies with the aim of testing two main working

51

hypothesis: 1) macroscopic anatomical features at the macroscale have a direct on impact the strain behaved by VICs at the cell scale, and 2) stress distribution through the leaflet thickness is strongly non-homogeneous if investigated at a level lower than the organ-scale.

3.2 Numerical multiscale workflow definition

The modeling workflow consists of three simulations at three different length-scales: organ (cm to mm), tissue (mm) and cell (μm). These are organized in a top-down scheme, so that each simulation provides data to feed the simulation at the immediately smaller length-scale, see Figure 3.1.

3.2.1 Organ length-scale model

The organ length-scale model of the AR is based on a refined version of the approach described in Chapter 2, which follows the same principal steps. For the sake of clarity the organ length-scale modeling is here briefly summarized again.

Acquisition of cMRI data and segmentation Cardiac magnetic resonance imaging (cMRI) was performed on 3 healthy volunteers (Table 3.1). T1-weighted cine-cMRI sequences were acquired on 18 planes evenly rotated around the axis passing through the center of the annulus and the center of the sino-tubular junction (Figure 3.2 A). Acquisitions were performed on a $1.5\,\text{T}$ Achieva scanner (Philips Healthcare Medical System, Irvine, Calif). In-plane spatial resolution and slice thickness were $1.1\,\text{mm}$ and $7\,\text{mm}$, respectively. Thirty frames/cardiac cycle were acquired with R-wave triggering. The segmentation and tracing of the images were performed following the same procedure described in Chapter 2.

	Subject 1	Subject 2	Subject 3
gender [M/F]	M	M	M
age [years]	28	31	27
weight [kg]	65	90	90

**Table 3.1:** *Table of Volunteers*

Reconstruction and discretization of AR geometry Manual tracings yielded a point-cloud, which was filtered to eliminate noise effects. A 3D surface
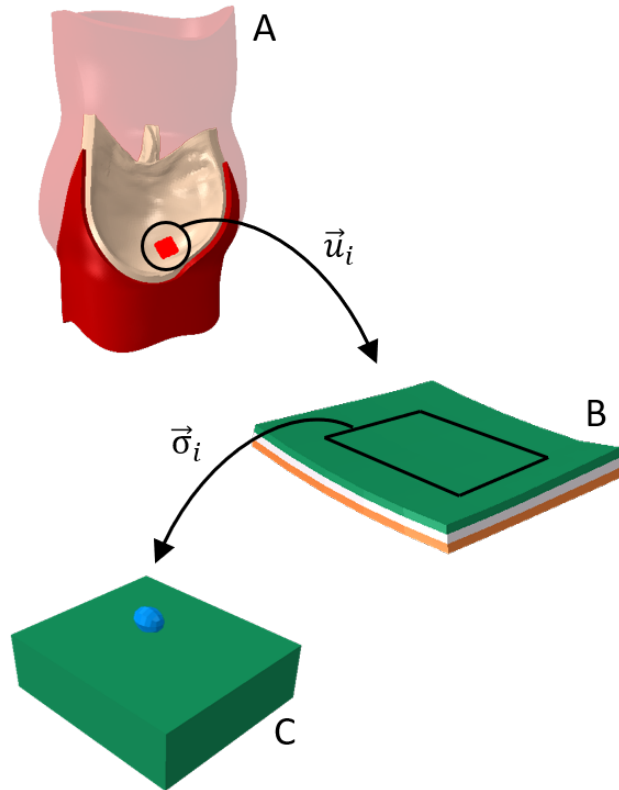
Figure 3.1: *Multiscale modeling approach. A) Organ length-scale. AR biomechanics is simulated over the cardiac cycle; a leaflet sub-region (bright red) is considered and the time-dependent nodal displacements ($\vec{\mu_i}$) at the boundary of the sub-region are extracted. B) Tissue length-scale. The leaflet sub-region is considered, and the layered structure of the tissue is accounted for (green = fibrosa, white = spongiosa, orange = ventricularis). The displacements $\vec{\mu_i}$ are used as boundary conditions and the time-dependent stresses ($\vec{\sigma_i}$) are extracted in the fibrosa layer, away from the boundaries (region silhouetted by the black line). C) The fibrosa layer is seeded with one VIC (highlighted in cyan) , the stresses $\vec{\sigma_i}$ are used as boundary conditions and the time dependents cell stretches are computed.*
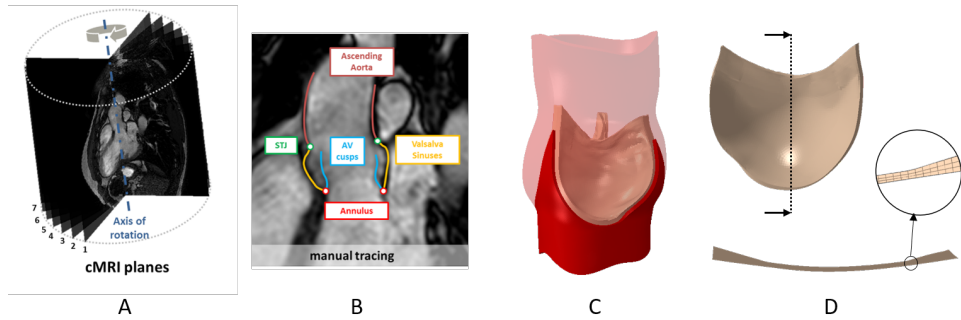
Figure 3.2: *A) cMRI planes (6 out of 18 planes are depicted). B) AR substructures manually traced on a cMRI plane. C) Reconstructed 3D geometry of the AR. D) Detail of an AV leaflet.*
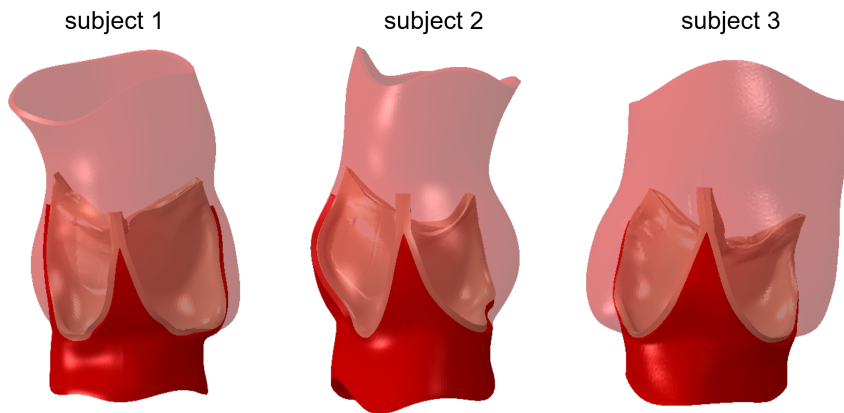
Figure 3.3: *The AR reconstructed models of the three subject.*

for each AR structure was created and discretized with quadrangular shell elements with characteristic dimension of $0.4\,\mathrm{mm}$ .The aortic wall volumetric mesh was obtained by the same process described in Chapter 2. The main difference form the previous reconstruction process is indeed the volumetric valve mesh. The leaflets volume mesh was obtained through an ad-hoc extrusion process in order to create a paradigmatic and region-dependent thickness pattern, ranging from $0.43\,\mathrm{mm}$ in the belly region to $1.2\,\mathrm{mm}$ at the attachment edge and at the free margin Grande et al. (1998), see Figure 3.2 D. Leaflets are described as layered, with the fibrosa, the spongiosa and the ventricularis accounting for 41%, 30% and 29% of the total thickness Stella and Sacks (2007).

	C[MPa]	b_1[−]	b_2[−]	b_3[−]	b_4[−]	K[MPa]
intact leaflet	2.82E-03	0.0	12.84	1.97	9.99	50
fibrosa	3.48E-06	5.49	81.48	-0.08	0.0	50
ventricularis	5.09E-06	4.86	5.02	-1.63E-03	0.0	50

Table 3.2: *Constitutive parameters for the intact leaflet used in the organ length-scale simulations and for the fibrosa and ventricularis layers used in the tissue length-scale simulations.*

Tissues mechanical properties   Aortic wall tissue was assumed linear, elastic and isotropic, with a $2\,\mathrm{MPa}$ Young's modulus and a 0.45 Poisson's ratio Conti et al. (2010), this assumption being necessary due to the setting of pre-stresses in Abaqus (see following paragraph). AV leaflet tissue was described as an anisotropic and hyperelastic, through the strain energy function U originally proposed by Guccione et al. (1991):

$$U = \frac{C}{2}(e^Q - 1) + K\left(\frac{J^2 - 1}{2} - lnJ\right) \tag{3.1}$$

where C is the first constitutive parameter, J the determinant of the deformation gradient tensor F, K is the bulk modulus and Q has the form:

$$\begin{aligned} Q =& 2b_1 Tr(E) + b_2 E_{ff} + \\ &+ b_3(E_{ss}^2 + E_{nn}^2 + E_{ns}^2 + E_{sn}^2) + \\ &+ b_4(E_{nf}^2 + E_{fn}^2 + E_{fs}^2 + E_{sf}^2) \end{aligned} \tag{3.2}$$

The terms E_{ij} are the components of the Green-Lagrange strain tensor, expressed with reference to a coordinate system f, s, n whose axes are aligned with preferentially oriented fibers (f) and orthogonally to them (n, s). In the model, f, s, n were considered aligned with the commissure-commissure, annulus-to-free margin and through-thickness direction, respectively. C and $b1, b2, b3, b4$ are the constitutive parameters, which were identified by least square fitting of experimental data from biaxial tensile tests by Stella and Sacks (2007), see Figure 3.4, and are reported in Table 3.2. The constitutive model was implemented into a VUANISOHYPER-STRAIN subroutine for the commercial solver ABAQUS Explicit (Dassault Systemes, Providence, RI, USA).
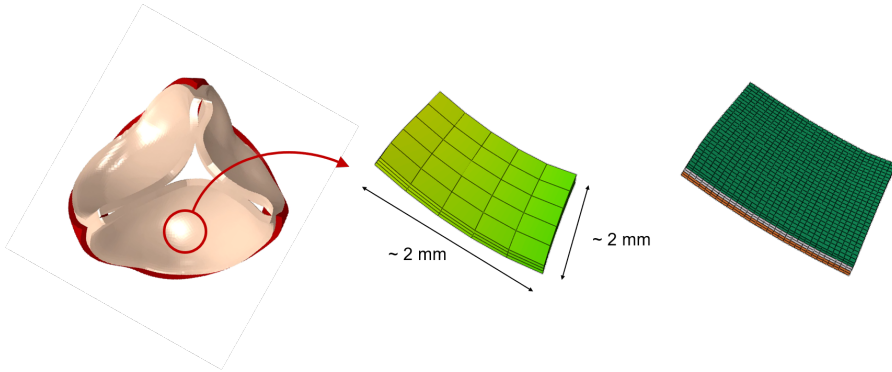
Computation of AV biomechanics   As for the organ level simulations of Chapter 2, the initial configuration of the AR was defined at early systole,
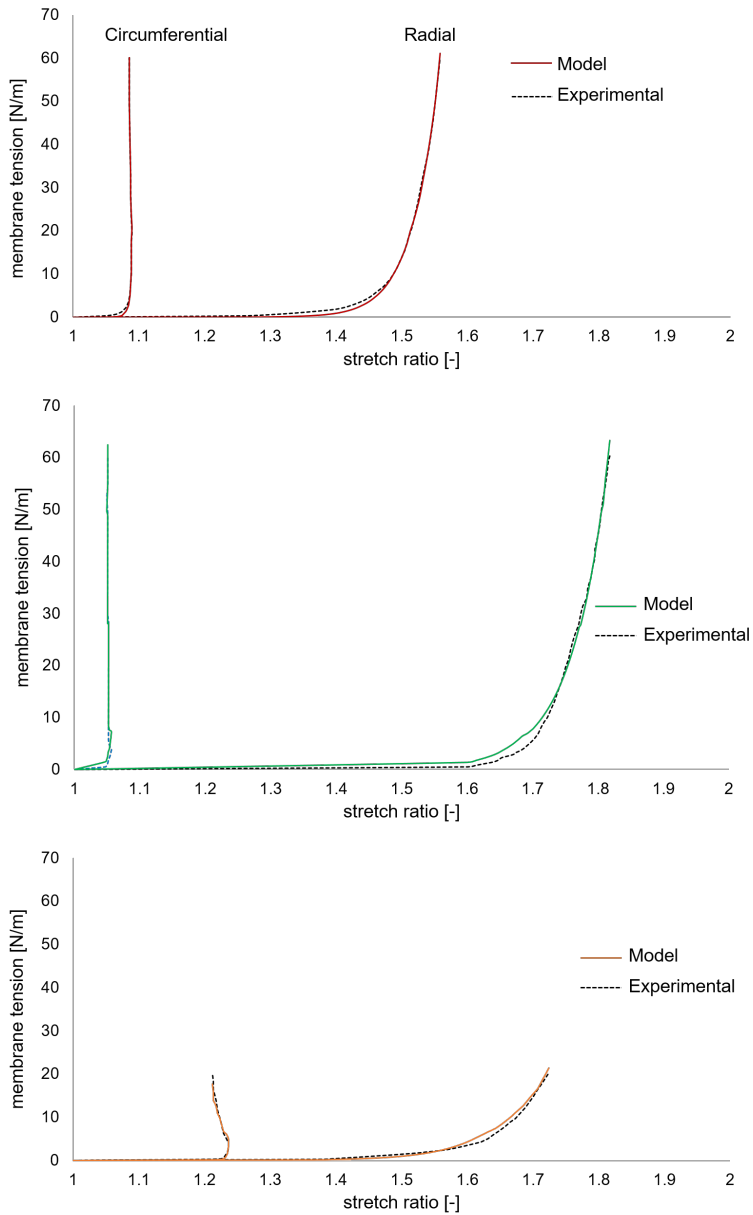
Figure 3.4: *Fitting of experimental data for the intact leaflet (top), fibrosa layer (middle) and ventricularis layer (bottom)*

Figure 3.5: *From the left to the right: the organ scale model, the selected patch with the original mesh and the remeshed patch with the layer-specific material definition.*

when AV leaflets are approximately unloaded, but the aortic wall is pressurized to $80\,\text{mmHg}$. Consistently, aortic wall pre-stresses the were computed through the iterative process described in Votta et al. (2017). Displacement boundary conditions were imposed to the nodes at the proximal and the distal ends of the AR model, so to allow only radial expansion or contraction of the AR wall. The structural response of the pre-stressed AR was computed over two consecutive cardiac cycles; to this aim, physiological time-dependent ventricular and aortic pressures were applied to the aortic wall upstream from and downstream of the AV, respectively, and a consistent trans-valvular pressure drop was applied to the AV leaflets. The circumferential and radial strains were averaged over a patch of $5 \times 5 \times 3$ elements ($\approx 2\,\text{mm}$ circumferential x $\approx 2\,\text{mm}$ radial x $0.43\,\text{mm}$ normal) in the central part of the belly region which experienced the highest strain values Labrosse et al. (2010).

3.2.2 Tissue length-scale model

Every leaflet patch selected at the organ scale was remeshed in order to refine the discretization while preserving its original shape. Every element of the organ scale patch (75 elements in total), was divided in 72 elements; to this aim, the position of the corresponding nodes was obtained by interpolation of the position of the original nodes of the element through the corresponding shape functions. This procedure yielded a new mesh of 5400 C3D8 elements, see Figure 3.5. The three different layers of the AV leaflets

were described through a dedicated mechanical characterization; for the fibrosa and the ventricularis layers we assumed an anisotropic and hyperelastic behavior, using the same formulation as in Equation 3.1. The model parameters were identified by least square fitting of experimental data from Stella and Sacks (2007) on the AV leaflets layers, see Figure 3.4 and are reported in Table 3.2. The spongiosa layer was described instead as linear, elastic and isotropic, with an elastic modulus of $0.02\,\mathrm{MPa}$ and a poisson ratio equal to 0.49. Displacement boundary conditions were applied to each outer node of the patch in order to reproduce the diastolic deformation behaved by the patch at the organ scale during the second cardiac cycle diastole. First, the stress-free patch was stretched to the configuration at beginning diastole, and then the full 3D diastolic displacement curve was applied. Circumferential and radial stress and strain data were then extracted in the central region of the for the fibrosa layer in order to avoid boundary effects.

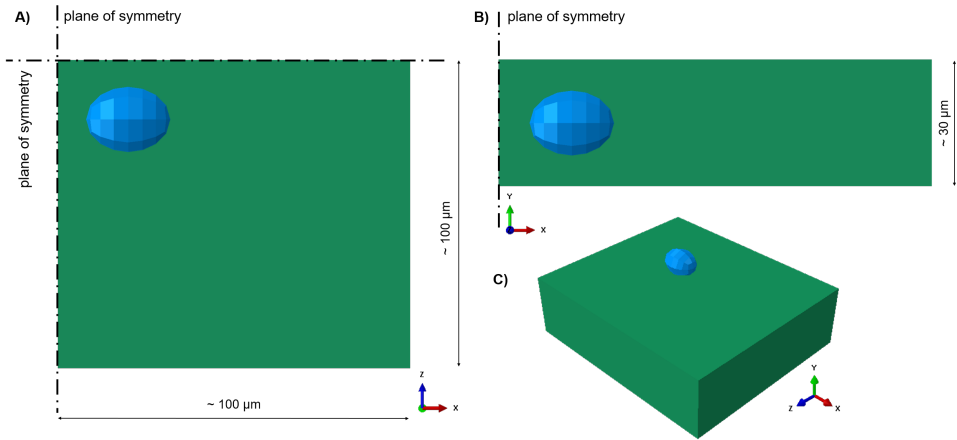### 3.2.3 Cell length-scale model

The cell scale model consists of a patch of fibrosa ECM with one embedded VIC . The constitutive model for the fibrosa ECM is the same of the tissue scale level. The cell is modeled as a linear, elastic and isotropic material with a Young modulus E = $9 \times 10^{-4}\,\mathrm{MPa}$ and a Poisson ratio $\nu = 0.45$ Huang (2004). The patch measured approximately $100\,\mu\mathrm{m}$ in the circumferential and radial direction and $30\,\mu\mathrm{m}$ in the normal direction and cell inclusion was embedded in the corner of the patch. Three planes of symmetry were defined on the computational domain, consisting of approximately 5200 C3D8 elements. Accordingly with experimental measurements from literature Huang (2004) the axes of the VIC were defined to be $10\,\mu\mathrm{m}$ in the circumferential direction and $7.7\,\mu\mathrm{m}$ in the radial and normal directions. Load boundary condition derived from the tissue scale simulations were applied in the circumferential and radial direction; the stress-free patch was pre-loaded using the stress field at the beginning of the diastole, then the tissue-derived stress curves were applied in the radial and circumferential direction respectively.

3.3 Results

3.3.1 Organ length-scale model

The AV biomechanics for the three subjects was evaluated on the second cardiac cycle simulated. In Figure 3.7 the contour plot of the circumfer-

Figure 3.6: *Top (A), side (B), and isometric (C) view of the cell length-scale patch.*

ential and radial strain of the belly region for each leaflet is represented. The highest strain values are concentrated in the belly region, while the attachment edge show almost no-deformation in both the circumferential and radial direction. AV strain highlighted the dependency on patient-specific anatomical features, in particular in the radial direction. Peak strain increased with leaflets surface and, since the 3 AV models did not share the same proportions between the extent of the 3 leaflets, different trends were obtained in terms of strain contour. For the circumferential direction however, the dependency of the strain contour on the anatomical features is less pronounced then for the radial direction. This effect is likely due to two principal effect: the presence of the fibers which are circumferentially oriented and the geometry of the AV itself, where the contact with the other leaflets prevents the circumferential deformation to reach a higher values, allowing indeed the belly region to bulge in the radial direction according to the leaflet extent. This behavior is even more clear considering the stretch ratios curves reported in Figure 3.8, and looking in particular to the the diastolic phase, i. e. the plateau part of the graphs. Here, despite the difference in the leaflets surface, the max circumferential strain range is very narrow and spans between 0.31 and 0.35, while the max radial strain ranges between 0.23 and 0.59. This effect is showed in the correlation plots between the leaflets surface and the circumferential and radial strain reported in Figure 3.9. For the circumferential direction the correlation returned a p-value $p = 0.0652$ and a $R^2 = 0.4053$, while in the radial direction we obtained $p = 0.0068$ and a $R^2 = 0.6728$.
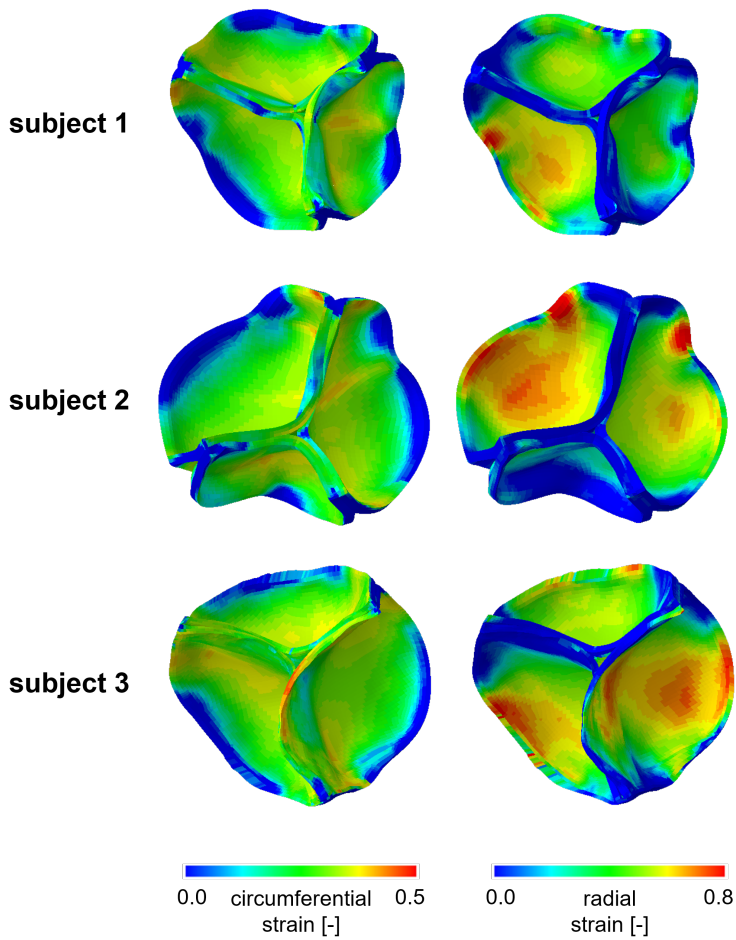
Figure 3.7: *Aortic view of the circumferential (right column) and radial (left column) strain computed on AV leaflets surface at peak diastolic transvalvular pressure for each simulated AV model.*
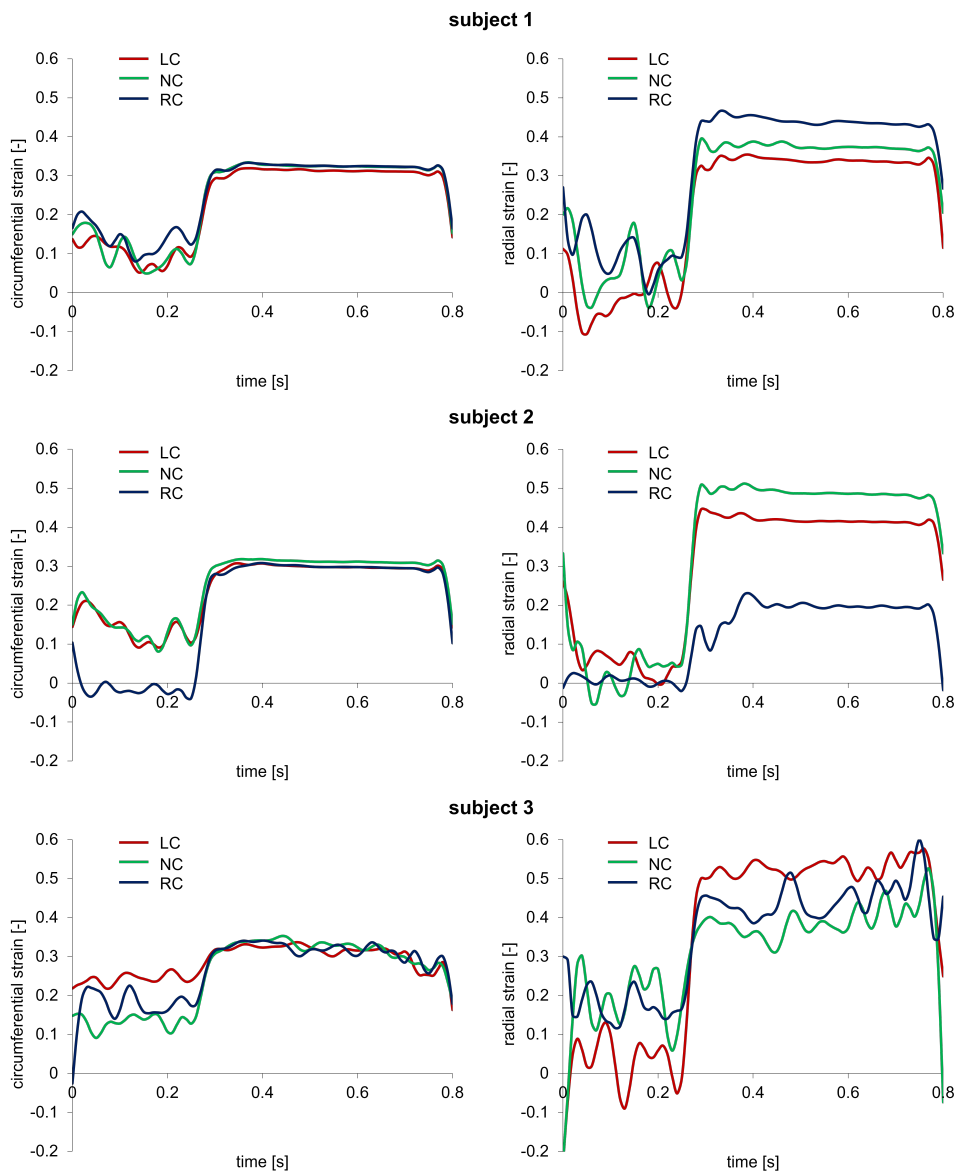
Figure 3.8: *Circumferential (left column) and radial (right column) stretch ratios in the center of the belly region of the left-coronary (LC), non-coronary (NC) and right-coronary (RC) leaflets over the cardiac cycle for the three subjects.*
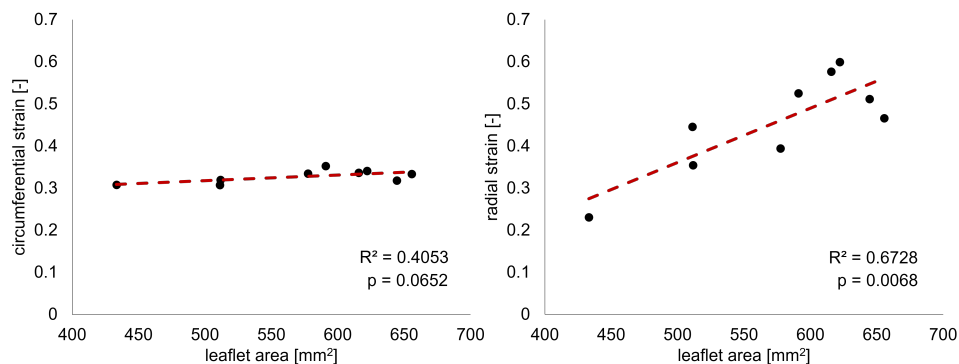
Figure 3.9: *The linear regression line and the corresponding p-value between the leaflet surface and the circumferential (left-hand side) and radial leaflet strain (right-hand side).*

3.3.2 Tissue length-scale model

The max principal stress was analyzed in order to check its distribution through the leaflet thickness. Due to the different mechanical proprieties assigned to each layer, a pronounced difference was highlighted, as depicted in Figure 3.10 for the LC leaflet of subject 1. The fibrosa layer showed to bear most of the leaflet's load compared to the spongiosa and ventricularis layers. Given that the fibrosa layer is the most prone to undergo tissue
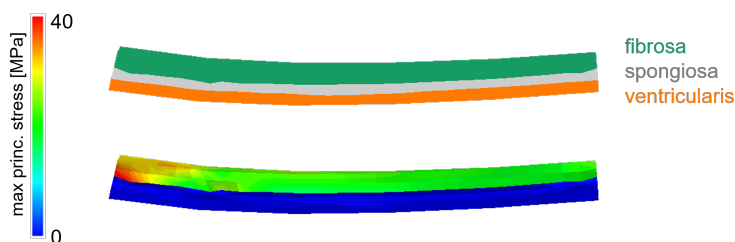
Figure 3.10: *Section of the LC leaflet patch of subject 1; the three different layer are represented on the top and the max principal stress through the thickness is plotted on the bottom.*

remodeling process, as already described before, the stress in the circumferential and radial direction were extracted from the pre-stressed patches just for this layer (Figure 3.11). The leaflet surface dependency of the radial strain value highlighted in Section 3.3.1 for the organ scale is at this scale visible in the stress curve extracted. At this scale it has to be remembered that the patches are pre-stretched in order to include the systolic phase de-

formation (as described in Section 3.2.2); this process impacts the stress curve generated as clearly visible for the RC leaflets of subject 2.

3.3.3 Cell length-scale model

Even if a complete mesh continuity exists between the VIC and the ECM, the difference in the mechanical proprieties between the two led to a discontinuity in the stress value at the interface, where the cell itself acts as a stress raiser. This behavior is depicted in Figure 3.12 for the LC leaflet of subject 1. The variation in length of the VIC long axis l_a (circumferential direction), and of the VIC short axis in the radial in the normal directions, s_a^{rad} and s_a^{norm} respectively, were computed over the diastolic phase. The cellular aspect ratio CAR^{rad} and CAR^{norm}, defined as the ratio between l_a and s_a^{rad}, and between l_a and s_a^{norm} respectively, are plotted in Figure 3.13. In Figure 3.14 the linear regression between the max strain at the organ scale-length and the max strain at the cell scale-length is reported. The narrow range in the circumferential direction noticed at the organ scale (see section 3.3.1), was found here for the cell scale, where the deformation ranges between 0.75 to 0.88. In the radial direction instead, as for the organ scale, the max strain range at the cell scale is wider, going from 0.36 to 0.87; the correlation between the organ scale deformations and the cell strain deformations gave a p-value < 0.0001 and $R^2 = 0.9521$, showing a high correlation between the two dataset (3.14).

3.4 Discussion

In the present study we developed a FE workflow for the multiscale analysis of the AV biomechanics, starting from subject-specific anatomies. To the best of our knowledge this is the first multiscale AV study able to transfer subject-specific macroscopic features down to the cell-scale. Moreover, a new way to concatenate boundary conditions was presented, making use of alternate displacement-stress BCs in order to guide the different length-scale simulations.

The strain curves computed during the cardiac cycle at the organ scale showed a good agreement with experimental data from M. Thubrikar (1979); only systolic strain in the circumferential direction slightly overestimated the corresponding experimental measurements. The highest strain values are concentrated in the belly region, while the attachment edge showed almost no-deformation in both the circumferential and radial direction, matching previous results reported in literature (Joda et al. (2016), Labrosse et al.
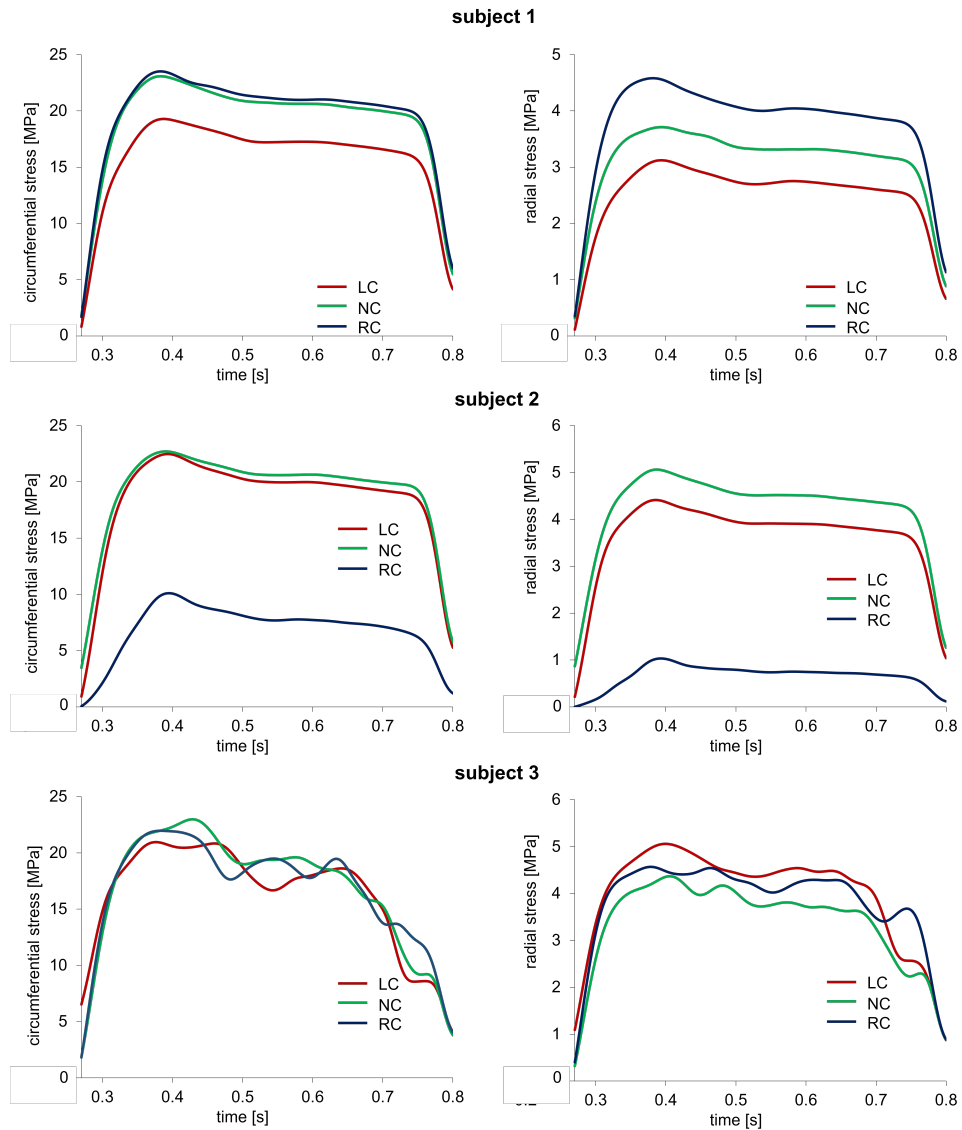
Figure 3.11: *Circumferential (left column) and radial (right column) stress in the fibrosa layer of the patch for the LC, NC and RC leaflets over the diastolic phase for the three subjects.*
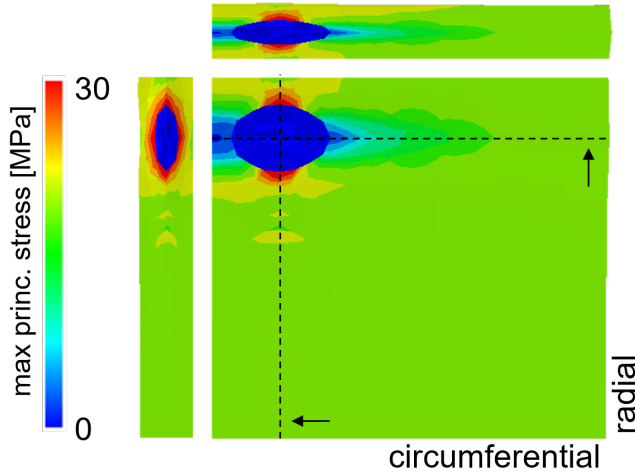
Figure 3.12: *Max principal stress on the cell length-scale model. The sections on the circumferential and radial plane are plotted on the top and left of the patch, respectively.*

(2010)). In the tissue-scale simulations we provide an insight of the strongly in-homogeneous stress distribution among the different AV leaflets layers. The fibrosa showed at the tissue level a load bearing role within the three AV layers, in agreement with Rego and Sacks (2017); this behavior is not observable from the homogeneous organ scale level and only a layer-dedicated mechanical description allows for this type of investigation. The normal CAR values measured at the plateau down at the cell scale are consistent with the CAR diastolic values predicted in the work of Weinberg and Mofrad (2007) from paradigmatic organ-scale models.

The impact of subject-specific leaflet extent on the leaflet strain at the organ level showed a correlation which was much more marked in the radial then in the circumferential direction, where a very narrow range in the max strain value was found despite the difference in the leaflets surface value. This, suggests that the radial one is the direction which is more influenced by anatomical difference in the leaflets shape. With the aim of studying the impact of subject-specific organ scale features on the cell-scale mechanical response we correlated the strain calculated at the organ level for each leaflet, to the corresponding strain measured in the cell level simulations. The correlation in the radial direction was much marked, while in the circumferential direction no correlation was found. This results support the findings of the work published by Lewinsohn et al. (2011), where
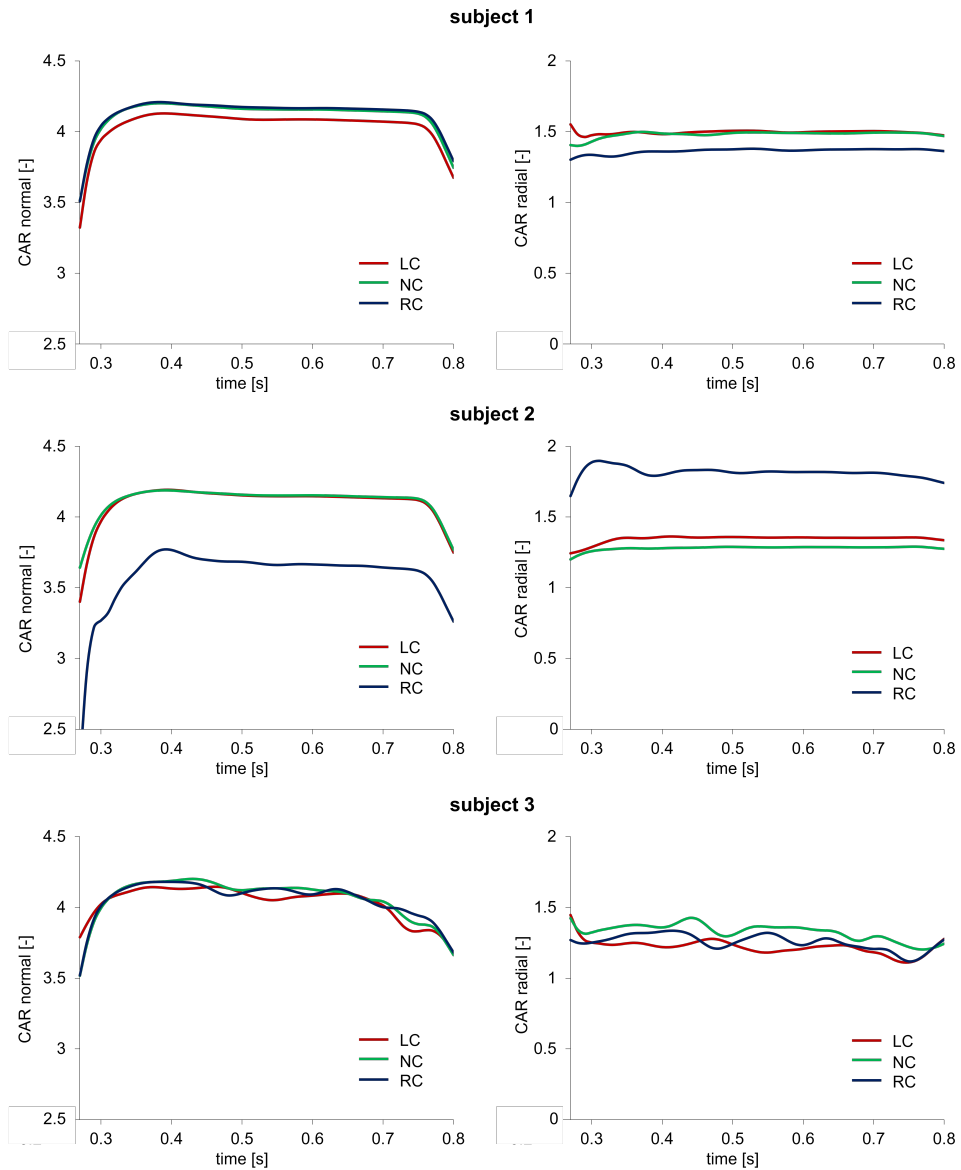
Figure 3.13: *Normal (left column) and radial(right column) CAR for the VIC inclusion of the LC, NC and RC leaflets over the diastolic phase for the three subjects.*
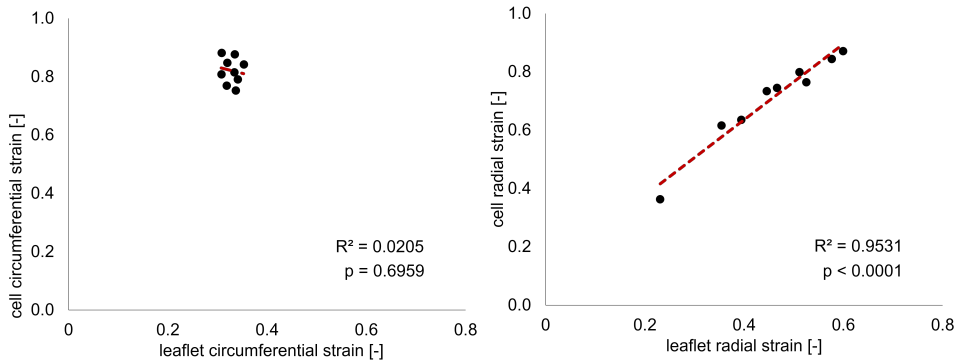
Figure 3.14: *The linear regression line and the corresponding R^2 and p-value between the leaflet and the cell strain in the circumferential (left-hand side) and radial direction (right-hand side).*

they suggest that the organization of matrix within the valve tissue acts to reduce direct tensile strain transfer to cells in the circumferential direction. Therefore, the radial directions appears as the one which is more sensible to anatomical leaflet differences, but in which this differences are transfer to the cell environment.

The most important limitation of this work is related to the leaflet thickness assessment. In fact, due to the low cMRI image resolution, a subject-specific thickness quantification from clinical images was not possible and the thickness value were taken from literature and set equal for all the leaflets. We can speculate that the thickness value depends directly on the leaflet extent: in particular we expect a thicker section for wider leaflets and a thinner section for the smaller ones in order to compensate the generation of deformation/stresses that fall out of an homeostasis range. The thickness value represents therefore and important variable in the model definition and our future efforts will be concentrated on changing the imaging technique in order to obtain subject-specific thickness data and consequently a more reliable organ scale geometry. The second limitation is related to the number of the subjects analyzed, which was limited to three; this small cohort prevent us to make general inferences from the results of our study, even if the FE workflow provided information which are consistent with the published literature.

In conclusion, the herein presented FE workflow allowed for the assessment of the multiscale biomechanical behavior of the AV from the organ level down to the cell scale; the workflow was applied to three physiological subjects anatomies. Indications on the effect of subject-specific anatom-

ical features at the organ scale down at the cell scale have been provided; these suggest a major role for the strain in the radial direction on the cell behavior, corroborating the findings of Lewinsohn et al. (2011).

Bibliography

Aikawa, E. and Libby, P. (2017). A rock and a hard place chiseling away at the multiple mechanisms of aortic stenosis. *Circulation*, 135(20):1951–1955.

Auricchio, F., Conti, M., Morganti, S., and Reali, A. (2014). Simulation of transcatheter aortic valve implantation: a patient-specific finite element approach. *Computer Methods in Biomechanics and Biomedical Engineering*, 17(12):1347–1357.

Billiar, K. L. and Sacks, M. S. (2000). Biaxial mechanical properties of the natural and glutaraldehyde treated aortic valve cusp–Part I: Experimental results. *Journal of biomechanical engineering*, 122(1):23–30.

Brazile, B., Wang, B., Wang, G., Bertucci, R., Prabhu, R., Patnaik, S. S., Butler, J. R., Claude, A., Brinkman-Ferguson, E., Williams, L. N., and Liao, J. (2015). On the Bending Properties of Porcine Mitral, Tricuspid, Aortic, and Pulmonary Valve Leaflets. *Journal of Long-Term Effects of Medical Implants*, 25(1-2):41–53.

Conti, C. A., Votta, E., Della Corte, A., Del Viscovo, L., Bancone, C., Cotrufo, M., and Redaelli, A. (2010). Dynamic finite element analysis of the aortic root from MRI-derived parameters. *Medical Engineering and Physics*, 32(2):212–221.

Gnyaneshwar, R. and Kumar, R. K. (2002). Original article : cardiovascular Dynamic analysis of the aortic valve using a finite. 73(4):3–6.

Grande, K. J., Cochran, R. P., Reinhall, P. G., and Kunzelma, K. S. (1998). Stress variations in the human aortic root and valve: The role of anatomic asymmetry. *Annals of Biomedical Engineering*, 26(4):534–545.

Guccione, J. M., McCulloch, A. D., and Waldman, L. K. (1991). Passive material properties of intact ventricular myocardium determined from a cylindrical model. *Journal of biomechanical engineering*, 113(1):42–55.

Huang, H.-y. S. (2004). Micromechanical simulations of heart valve tissues. *Bioengineering*.

Joda, A., Jin, Z., Haverich, A., and Summers, J. (2016). Multiphysics simulation of the effect of leaflet thickness inhomogeneity and material anisotropy on the stressâstrain distribution on the aortic valve. *Journal of Biomechanics*, 49(12):2502–2512.

Kim, H., Chandran, K. B., Sacks, M. S., and Lu, J. (2007). An experimentally derived stress resultant shell model for heart valve dynamic simulations. *Annals of Biomedical Engineering*, 35(1):30–44.

Labrosse, M. R., Lobo, K., and Beller, C. J. (2010). Structural analysis of the natural aortic valve in dynamics: From unpressurized to physiologically loaded. *Journal of Biomechanics*, 43(10):1916–1922.

Lee, C. H., Carruthers, C. A., Ayoub, S., Gorman, R. C., Gorman, J. H., and Sacks, M. S. (2015). Quantification and simulation of layer-specific mitral valve interstitial cells deformation under physiological loading. *Journal of Theoretical Biology*, 373:26–39.

Lewinsohn, A. D., Anssari-Benham, A., Lee, D. A., Taylor, P. M., Chester, A. H., Yacoub, M. H., and Screen, H. R. C. (2011). Anisotropic strain transfer through the aortic valve and its relevance to the cellular mechanical environment.

M. Thubrikar, W. C. Piepgrass, T. W. S. S. P. N. (1979). *Surgical Forum*, (30):241–243.

Merryman, W. D., Youn, I., Lukoff, H. D., Krueger, P. M., Guilak, F., Hopkins, R. A., and Sacks, M. S. (2005). Correlation between heart valve interstitial cell stiffness and transvalvular pressure: implications for collagen biosynthesis. *American Journal of Physiology-Heart and Circulatory Physiology*, 290(1):H224–H231.

Otto, C. M. (2002). Calcification of bicuspid aortic valves. *Heart*, 88(4):321–322.

Rego, B. V. and Sacks, M. S. (2017). A functionally graded material model for the transmural stress distribution of the aortic valve leaflet. *Journal of Biomechanics*, 54:88–95.

Rutkovskiy, A., Malashicheva, A., Sullivan, G., Bogdanova, M., Kostareva, A., Stensløkken, K. O., Fiane, A., and Vaage, J. (2017). Valve interstitial cells: The key to understanding the pathophysiology of heart valve calcification. *Journal of the American Heart Association*, 6(9):1–23.

Sacks, M. S. and Yoganathan, A. P. (2007). Heart valve function: A biomechanical perspective. *Philosophical Transactions of the Royal Society B: Biological Sciences*, 362(1484):1369–1391.

Stella, J. A. and Sacks, M. S. (2007). On the Biaxial Mechanical Properties of the Layers of the Aortic Valve Leaflet. *Journal of Biomechanical Engineering*, 129(5):757.

Taylor, P. M., Batten, P., Brand, N. J., Thomas, P. S., and Yacoub, M. H. (2003). The cardiac valve interstitial cell. *International Journal of Biochemistry and Cell Biology*, 35(2):113–118.

Votta, E., Presicce, M., Della Corte, A., Dellegrottaglie, S., Bancone, C., Sturla, F., and Redaelli, A. (2017). A novel approach to the quantification of aortic root in vivo structural mechanics. *International Journal for Numerical Methods in Biomedical Engineering*, 33(9):1–22.

Weinberg, E. J. and Mofrad, M. R. K. (2007). Three-dimensional, multiscale simulations of the human aortic valve. *Cardiovascular Engineering*, 7(4):140–155.

Weinberg, E. J., Shahmirzadi, D., Mohammad, ·., and Mofrad, R. K. (2010). On the multiscale modeling of heart valve biomechanics in health and disease. *Biomech Model Mechanobiol*, 9:373–387.

Chapter 4

Tensor mapping for AV fiber structural data

This chapter was based on:

W. Zhang, G. Rossini, T. Bui-Thanhc, M. S. Sacks, **The integration of structure and high-fidelity material models in heart valve simulations using machine learning**, Under submission on the Journal of Computer Methods in Applied Mechanics and Engineering.

4.1 Introduction

Heart valve leaflets are layered tissues mainly composed of collagen and elastin fibers (see Section 1.1.3). This fibrous architecture thus dictates the direction and degree of mechanical anisotropy, as well as the overall mechanical responses (Driessen et al. (2005)). However, this information is not available from in-vivo measures and must be acquired from excised tissues. Although the gold standard for micro-structural assessment of tissues is considered the histology, alternative imaging techniques have been explored in to study fibre organization in soft tissues. The most common ones are polarised ligth microscopy (PLM) (Canham et al. (1989), Sáez et al. (2016)) and electron microscopy (EM) (Frank et al. (1991), Dahl et al. (2007)). However, these techniques are destructive for the tissue and are time-consuming due to the complex tissue preparation. Therefore non-destructive techniques preserving the sample such as multiphoton microscopy (Cicchi et al. (2009)) or confocal microscopy (O'Connell et al. (2008)) are becoming more popular. Despite the advantages, these techniques have a low depth of penetration and they are not suitable for assessing the fiber structure of a whole AV leaflet. In this context Small Angle Light Scattering (SALS) may represent a good alternative for assessing fibre structure *ex vivo* across large regions of AV leaflets without the need for complex and time consuming preparation steps: in this technique the light passes orthogonally through the tissue specimen in a non-destructive way, allowing to reconstruct the collagen fiber structure without damaging the leaflet tissue. Laser light is passed through a tissue specimen, and the spatial intensity distribution of the resulting scattered light represents the sum of all structural information. This experimental method, used for the characterization of fibers structure of several biological tissues, was specialized by Sacks et al. (1997)) for heart valve tissues (figure 4.1), allowing for rapid data acquisition and automated high spatial resolution specimen positioning, and has been used in several studies, such as in Padala et al. (2010), Aggarwal et al. (2014) and Gaul et al. (2017) . Despite the experimental possibility to assess the fiber structure of an excised AV leaflet, to the best of our knowledge there is no evidence in the literature of a mapping technique allowing to smoothly transfer the in-vitro collagen fiber orientation to any in-vivo measured leaflet geometry, ready to be used for subsequent numerical studies.

To address this limitation we developed a novel structural tensor method to represent fiber orientation probability density functions (ODFs). This approach allows for efficient representation and tensor coordinate transfor-
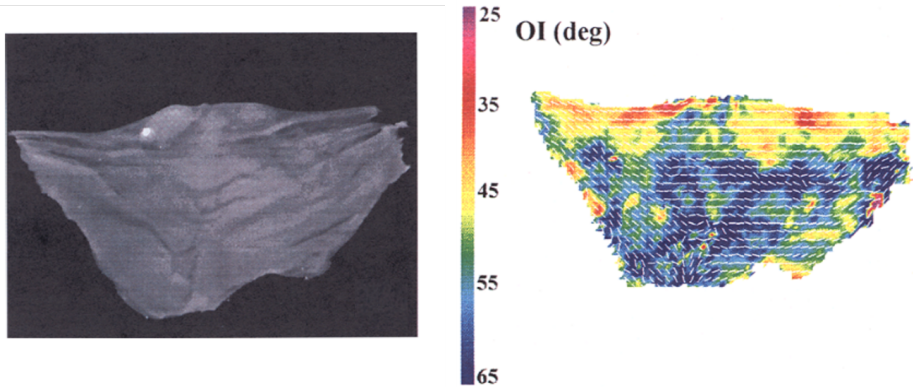
Figure 4.1: *Gluteraldehyde fixed porcine AV leaflet (left side) and corespondent SALS obtained Orientation Index for the collagen fibers in degree (right side).*

mation to facilitate mapping from experimental data to NURBS based representations of heart valve leaflet geometry. For the description and subsequent mapping of ODFs we exploited the high order structural tensors (HOST) representation technique presented in section 4.2. We demonstrate the approach with human derived normal and BAV leaflet structural data taken from Aggarwal et al. (2014). In the latter the averaged structure of human normal and bicuspid leaflets in the early disease stage was quantified. Interestingly, they did not find significant differences in the mean fiber direction in two cases which suggests that on a coarse scale, the fibers are still running predominantly along the circumferential direction. However, for BAV leaflets a disorganized structure was demonstrated showing that collagen fiber architecture becomes less aligned (Figure 4.2). The regularity in the observed micro-structure in the measured population suggests that *consistent population based metrics* for the human population from ex-vivo tissues can be used in patient-specific simulations.

4.2 High Order Structural Tensors (HOST) to represent in planar fiber orientation

The orientation distribution function, $\Gamma(\mathbf{X}, \mathbf{n})$, is a probability distribution function that describes the angular distribution of a species (in this application, a fiber population in a biological soft tissue specimen), where x is the 3-D position vector and $\mathbf{n}$ is the orientation vector, $\mathbf{n} = \mathbf{n}(\theta)$. Note that we describe the orientation distribution function as $\Gamma(\mathbf{n})$ when we are referring to it generally and not at a specific spatial coordinate, $\mathbf{x}$. From $\Gamma(\mathbf{n})$,
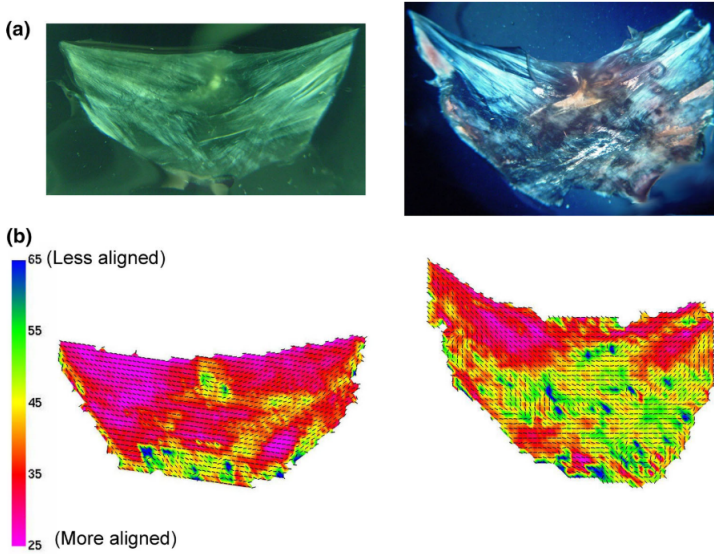
Figure 4.2: *(a) Collagen architecture visible in TAV and BAV leaflets under polarized light and (b) quantified fiber architecture for representative TAV and BAV leaflets using SALS setup Aggarwal et al. (2014)*

we acquire the preferred direction which describes the primary direction of the fiber population and can be represented as scalar angle value θ_p. We start by establishing some basic characteristics of $\Gamma(\mathbf{n})$. Due to the inherent symmetries in any fiber distribution, $\Gamma(\mathbf{n})$ will be a symmetric function so that

$$\Gamma(\mathbf{n}) = \Gamma(-\mathbf{n}), \tag{4.1}$$

with normalization requiring that

$$\int_{-\pi/2}^{\pi/2} \Gamma(\mathbf{n})d\theta = 1. \tag{4.2}$$

From $\Gamma(\mathbf{n})$, several key fiber orientation characteristics can be derived as follows. The preferred direction which describes the primary direction of the fiber population and is determine using

$$\mathbf{n}_p = \int_{-\pi/2}^{\pi/2} \Gamma(\mathbf{n})\,\mathbf{n}\,d\mathbf{n}. \tag{4.3}$$

We also determine an orientation index (ν), a normalized measure of the degree of alignment, where 0 represents random of the fibers (i.e. if $\Gamma(\mathbf{n})$

were a uniform distribution) and a value of 100 represents all of the fibers being in perfect alignment.

$$\nu[\Gamma(\mathbf{n})] = 100 \cdot \left(\frac{\sigma_{MAX} - \sigma)}{\sigma_{MAX}}\right) \tag{4.4}$$

$$\sigma = \sqrt{\int_{-\pi/2}^{\pi/2} (\mathbf{n} - \mathbf{n}_p)^2 \Gamma(\mathbf{n}) d\mathbf{n}} \tag{4.5}$$

$$\sigma_{MAX} = \sqrt{\int_{-\pi/2}^{\pi/2} \frac{\theta^2}{\pi/2} d\theta} \tag{4.6}$$

Since we are dealing with planar tissues we restrict ourselves to in-plane 2D fibrous structures only. A Fourier series was used to represent $\Gamma(\mathbf{X}, \mathbf{n})$ efficiently; this formulation was also useful for structural tensor representation, as presented below. The Fourier series is given by

$$\Gamma[\mathbf{n}(\theta)] = \frac{1}{2\pi} \left[1 + \sum_{j=1}^{7} a_{2j} cos(2j\theta) + b_{2j} sin(2j\theta) \right]. \tag{4.7}$$

Structural tensors have a long history in the analysis of texture in materials. General frameworks have been formulated for a wide range materials for 3D distributions based on spherical harmonics (Kanatani (1984)) and planar distributions using Fourier series (Advani and Tucker (2002)). The research group of Prof. M. S. Sack at the J.T. Willerson Center for Cardiovascular Modeling and Simulation at the University of Texas in Austin (Austin, TX, USA), specialize and extend these approaches for soft tissue representations. In the following this representation was numerically implemented together and the overall tensor mapping process from the experimental data to the 3D NURBS geometry was developed. A 14th-order Fourier series was selected, as it was shown to successfully capture $\Gamma(\mathbf{X}, \mathbf{n})$ for all valvular tissues studied, with a Pearson's correlation coefficient of 0.95 or better. A generalized approach which utilizes the relation between a 2D structural tensor of any order based on a Fourier series representation (eqn. 4.7) was used.

We first define the $D_{i_1, i_2, ..., i_n}$ as an nth rank deviator tensor termed a "fabric tensor of the third kind" (Kanatani (1984)) with $D_0 = 1$ to satisfy the normalization requirement in eqn. 4.2. It can be shown for any order n $D_{i_1, i_2, ..., i_n}$ that

$$D_{i_1, i_2, ..., i_m} = \begin{cases} (-1)^{k/2} a_n & k : even \\ (-1)^{(k-1)/2} b_n & k : odd \end{cases} \tag{4.8}$$

(a) $D_{i_1 i_2 i_3 i_4}$	k	Independent component	value
D_{1111}	0	c_1	a_4
D_{1112}	1	c_2	b_4
D_{1122}	2	c_3	$-a_4$
D_{1222}	3	c_4	$-b_4$
D_{2222}	4	c_5	a_4

(b)

$$\left(\begin{array}{cc} \begin{pmatrix} c1 & c2 \\ c2 & c3 \end{pmatrix} & \begin{pmatrix} c2 & c3 \\ c3 & c4 \end{pmatrix} \\ \begin{pmatrix} c2 & c3 \\ c3 & c4 \end{pmatrix} & \begin{pmatrix} c3 & c4 \\ c4 & c5 \end{pmatrix} \end{array} \right)$$

Figure 4.3: *(a) Example showing the five independent component values for a fourth rank fabric tensor of the third kind in terms of the Fourier series coefficients. (b) The values in terms of the five independent Fourier series components $c_1 - c_5$ for the 4th rank fabric tensor D_{i_1, i_2, i_3, i_4}*

were a_n and b_n are the Fourier series coefficients in eqn. 4.7 and k is the number of times the value "2" is repeated in the indexes (e.g.: if $D = D_{1,2,2,2}$, so $k = 3$). The remaining terms can be determined by symmetry. For example, for the five independent components $c_1 - c_5$ the complete is shown in Figure 4.3. Thus for the fourth rank which has sixteen components, only five are independent and determined directly from the Fourier coefficients as shown above. Similar expressions can be obtained for D of any rank m. The ODF can then be recovered using

$$\Gamma(\mathbf{n}) = \frac{1}{2\pi}(D_0 + D_{i_1 i_2} n_{i_1} n_{i_2} + D_{i_1 i_2 i_3 i_4} n_{i_1} n_{i_2} n_{i_3} n_{i_4} + + D_{i_1 i_2 i_m} n_{i_1} n_{i_2} n_{i_m})$$

This approach worked very well for more aligned tissues, such as those found in valvular tissues (Figure 4.4). Once $\Gamma(\mathbf{X}, \mathbf{n})$ is represented, it is commonly required to determine the axes of symmetry of $\Gamma(\mathbf{X}, \mathbf{n})$. This is easily done using the eigenvalues of the second rank structural tensor $D_{i_1 i_2}$, which acts essentially as a low-pass filter. The resulting eigenvectors indicate axes of symmetry for $\Gamma(\mathbf{X}, \mathbf{n})$ (Fig. 4.5).

4.2.1   Coordinate transformations

One major benefit of the structural tensor approach is that it facilitates coordinate system transformation of $\Gamma(\mathbf{X}, \mathbf{n})$. To do this, we assume that the any
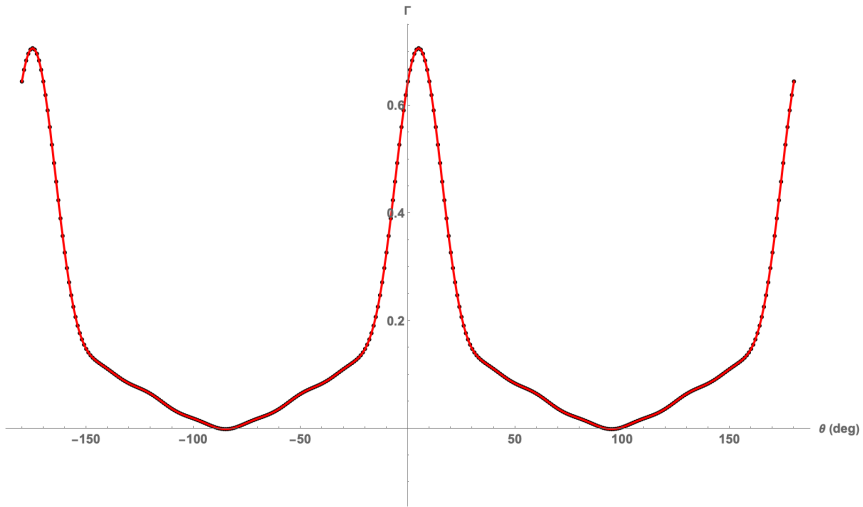
Figure 4.4: *Example of the 14th rank structural tensor for valvular tissue, showing an excellent fit.*
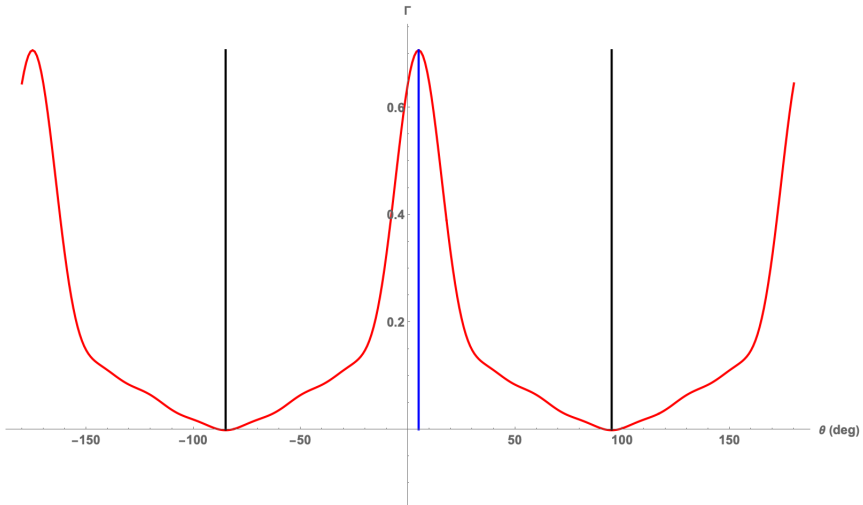
Figure 4.5: *Example the axes of symmetry as determined by eigenvectors of second rank structural tensor $D_{i_1 i_2}$ for the $\Gamma(\mathbf{X}, \mathbf{n})$ shown in Fig. 4.4. The blue and black lines represent the first and second eigenvectors, respectively.*

coordinate mapping can be described at each point $\mathbf{X}$ using a deformation gradient tensor $\mathbf{F}(\mathbf{X})$. Next, we separate the deformation and rigid body rotation components using polar decomposition $\mathbf{F} = \mathbf{R} \cdot \mathbf{U}$, where $\mathbf{R}$ is the orthogonal rotation and $\mathbf{U}$ the stretch tensors, respectively. We transform $\Gamma(\mathbf{X}, \mathbf{n})$ in two steps. First, under the assumption of affine transformation, $\Gamma(\mathbf{X}, \mathbf{n})$ in the deformed (but not rotated) state can be determined using Fan and Sacks (2014).

$$\Gamma'(\mathbf{n}) = \Gamma(\mathbf{n}) \frac{\mathbf{n} \cdot \mathbf{Cn}}{J} \tag{4.9}$$

where $J = det[\mathbf{U}]$ and $\mathbf{C} = \mathbf{U}^2$. Once $\Gamma'(\mathbf{n})$ has been determine, the Fourier series and structural representation are determined as presented above. Next, the resultant structural tensors $D_{i_1 i_2 i_m} n_{i_1} n_{i_2} ... n_{i_m}$ are transformed using $\mathbf{R}$ and standard tensor coordinate transformation rules. For example, the 4th rank fabric tensor expressed in the mapped coordinate system D'_{i_1, i_2, i_3, i_4} can be determined using

$$D'_{i_1, i_2, i_3, i_4} = R_{i_1, j_1} R_{i_2, j_2} R_{i_3, j_3} R_{i_4, j_4} D_{j_1, j_2, j_3, j_4} \tag{4.10}$$

and the final form of $\Gamma(\mathbf{n})$ determined using eqn. 4.2. This approach can thus represent complex, generalized forms of $\Gamma(\mathbf{n})$ with only 14 parameters and facilitates straightforward geometric mapping using conventional tensor coordinate transformations, as presented in the following section.

4.3 Tri-leaflet geometric representation

The methods for the formulation of the NURBS based representation of a tri-leaflet heart valve was presented in Xu et al. (2018). Briefly, starting from the NURBS surface representation of the geometry used in Sun et al. (2005), valve leaflets were parametrically designed by picking nine "key points" located on the ends of commissure lines and the bottom of the sinuses. This method was used to parametrically change the free edge and belly curve and therefore change the valve design to match the shape of the valve taken from Sun et al. (2005). This procedure was implemented in an interactive geometry modeling and parametric design platform based on Rhinoceros 3D and Grasshopper (www.rhino3d.com).

4.4 Mapping to NURBS leaflet representation

To demonstrate our ability to map complex heart valve fiber structures, we used results for the normal and bicuspid heart valve Aggarwal et al. (2014).

Of particular interest is that the fiber data represents a population average and thus underscores the potential for utilizing such information in both patient-specific and population applications. Details of the methodologies and patient selection criteria have been previously presented in Aggarwal et al. (2014). Briefly, explanted human normal and bicuspid aortic valve leaflets were excised during post-surgically, processed, and laid flat so that the (collagen) fiber orientation distribution $\Gamma(\mathbf{X}, \mathbf{n})$ at each measurement point $\mathbf{X}$ was quantified using a dense measurement 2D grid ($250 \, \mu$m spacing) over entire leaflet surface. The resulting data from each leaflet were mapped to a common geometric representation to facilitate group (i.e. normal and bicuspid) averages. Interestingly, statistically different and consistent regional structures were found between the normal and bicuspid valves. The regularity in the observed micro-structure is an essential cornerstone of any predictive mathematical models of valve disease. It was for this reason we utilized these data in the present study. Starting with the resulting 2D group averages, we mapped this structural data onto a 3D NURBS parametric leaflet geometry, obtained from the formulation of the NURBS based representation of a tri-leaflet heart valve presented in [9]. We note that the corresponding 3D NURBS surface control points were defined on the 2D template geometry using a technique similar to the one described in Aggarwal et al. (2014), in keeping the same global parameter knot space of the 3D leaflet NURBS geometry $(u, v) = [0, 1] \times [0, 1]$ (Figure 4.6). Thus, instead of directly fitting a surface we first identified the two commissures and fitted two C^1 continuity open spline curves to the free edge and the attachment edge, respectively. Then a ruled NURBS surface was created between the two open curves. This process guarantee the same control points net on both geometry, easing the following computation of the deformation gradient tensor $\mathbf{F}_{map}$. Due to the high data resolution of the measured fiber architecture data it was possible to precisely map the transformed $\Gamma(\mathbf{n})$ to each control point of the 2D surface using the HOST technique described in Section 4.2. Then, the mapping deformation gradient tensor $\mathbf{F}_{map}$, representing the transformation matrix between the two configuration, was determined at each map point between the two NURBS surface. Once the transformation tensors were generated, they had to be applied to the tensor representation of the structural data. Note that in this application only rotation was required so that $\mathbf{U}_{map} = \mathbf{I}$ and $\mathbf{F}_{map} = \mathbf{R}_{map}$, where $\mathbf{I}$ is the identity tensor. From the transformed structural tensors the Fourier Series coefficients in the mapped coordinate system were calculated and the new ODF $\Gamma_{map}(\mathbf{X}, \mathbf{n}')$ was reconstructed. From the resulting $\Gamma_{map}(\mathbf{X}, \mathbf{n}')$ the fiber population preferred direction and standard device
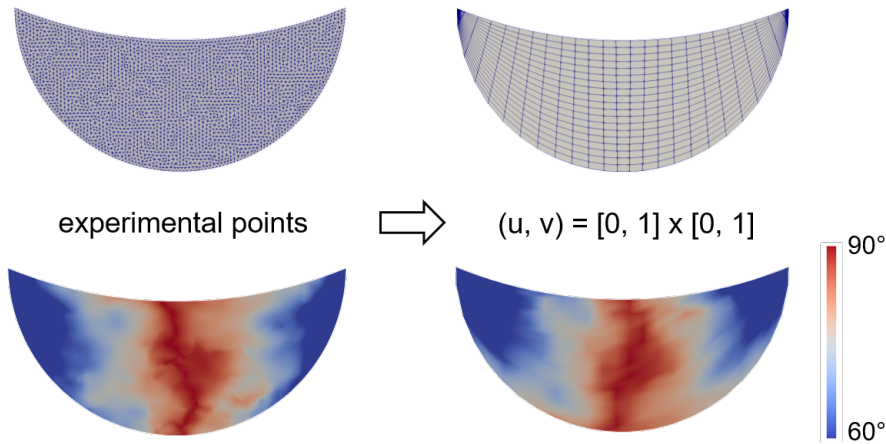
Figure 4.6: *From the left: the 2D grid of the experimental SALS data and the 2D NURBS fitted surface.*

were determined as described in section 4.2, completing the mapping process. The results of the mapping are presented in Figure 4.7 both for the normal AV and the BAV, together with the starting 2D averaged SALS data from Aggarwal et al. (2014). The resulting ODFs are reasonable estimations and in addition, we checked that the resulting ODFs are non-negative and sum to 1 after the transformation at each NURBS control point.

4.5 Discussion

This work aimed at developing a structural tensor method to represent fiber orientation functions ODFs, allowing for efficient data representation and easy tensor coordinate transformation. To this aim we made use of the structural tensor theory originally proposed by Kanatani (1984) and Advani and Tucker (2002) and of its extension and specialization to the soft tissue representation developed at the J.T. Willerson Center for Cardiovascular Modeling and Simulation by the research group of Prof. M. S. Sacks. On the top of this theory we developed a mapping technique able to easily transform ODFs data from a 2D geometry onto a 3D geometry via NURBS parametric space. The mapping procedure was tested using experimental data on normal AV and BAV form Aggarwal et al. (2014) as a starting point, performing the mapping to a 3D NURBS parametric geometry. To the best of our knowledge our approach yielded the first technique making use of tensor representation to map ODF information between two different
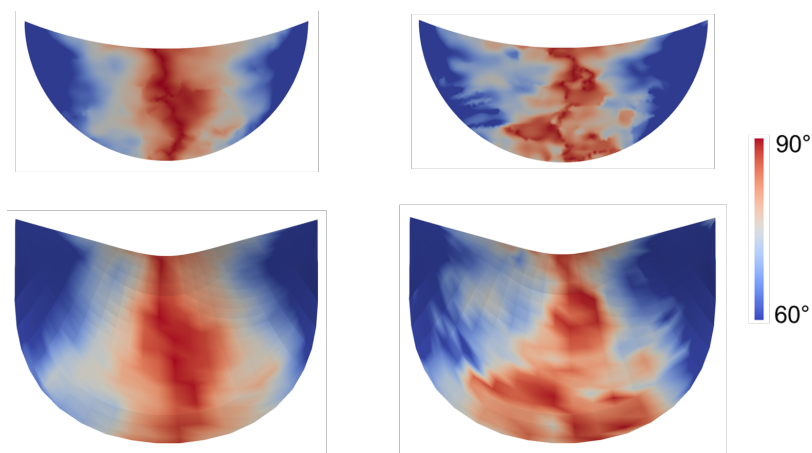
Figure 4.7: *The fiber angle α mapped from the 2D geometry, top line, to the 3D NURBS leaflet surface, bottom line both for the normal valve (left side) and the bicuspid valve (right).*

NURBS geometry configuration, starting form a Fourier series description of the ODF itself.

Despite our encouraging results, some limitations of the proposed approach should be highlighted. Both are related to the geometry used. The first one is related to fact that the model was paradigmatic and very simplified. However, it has to be noted that the mapping process could be performed to any NURBS described 3D geometry, even a patient-specific geometry directly derived from standard clinical imaging techniques (e.g.: MRI, CT scan, Echocardiography). For that reason, for the next future we plan to perform the mapping on more complex image-derived 3D NURBS models, to further test our method on a real AV geometry. The second limitation is related to the need to introduce thickness in the leaflet geometrical description in order not only to be able to capture difference in the stress strain throughout the thickness itself, but also to get a model which could be used as the first step in the multiscale workflow developed in Chapter 3.

Bibliography

Advani, S. G. and Tucker, C. L. (2002). The Use of Tensors to Describe and Predict Fiber Orientation in Short Fiber Composites. *Journal of Rheology*, 31(8):751–784.

Aggarwal, A., Ferrari, G., Joyce, E., Daniels, M. J., Sainger, R., Gorman, J. H., Gorman, R., and Sacks, M. S. (2014). Architectural Trends in the Human Normal and Bicuspid Aortic Valve Leaflet and Its Relevance to Valve Disease. *Annals of Biomedical Engineering*, 42(5):986–998.

Canham, P. B., Finlay, H. M., DIXON, J. G., Boughner, D. R., and Chen, A. (1989). Measurements from light and polarised light microscopy of human coronary arteries fixed at distending pressure. *Cardiovascular Research*, 23(11):973–982.

Cicchi, R., Kapsokalyvas, D., De Giorgi, V., Maio, V., Van Wiechen, A., Massi, D., Lotti, T., and Pavone, F. S. (2009). Scoring of collagen organization in healthy and diseased human dermis by multiphoton microscopy. *Journal of Biophotonics*, 3(1-2):34–43.

Dahl, S. L. M., Vaughn, M. E., and Niklason, L. E. (2007). An Ultrastructural Analysis of Collagen in Tissue Engineered Arteries. *Annals of Biomedical Engineering*, 35(10):1749–1755.

Driessen, N. J. B., Bouten, C. V. C., and Baaijens, F. P. T. (2005). Improved Prediction of the Collagen Fiber Architecture in the Aortic Heart Valve. *Journal of Biomechanical Engineering*, 127(2):329.

Fan, R. and Sacks, M. S. (2014). Simulation of planar soft tissues using a structural constitutive model: Finite element implementation and validation. *Journal of Biomechanics*, 47(9):2043–2054.

Frank, C., MacFarlane, B., Edwards, P., Rangayyan, R., Liu, Z.-Q., Walsh, S., and Bray, R. (1991). A quantitative analysis of matrix alignment in ligament scars: A comparison of movement versus immobilization in an immature rabbit model. *Journal of Orthopaedic Research*, 9(2):219–227.

Gaul, R., Nolan, D., and Lally, C. (2017). Collagen fibre characterisation in arterial tissue under load using SALS. *Journal of the Mechanical Behavior of Biomedical Materials*, 75:359–368.

Kanatani, K.-i. (1984). DISTRIBUTION OF DIRECTIONAL DATA Cijknifljnk [C + Cini t Cijninj t Cijkninjnk t ' ' ' I *, (III) exp [C t Cini t Cijflinj t Cijkninjnk. 12(2):149–164.

O'Connell, M. K., Murthy, S., Phan, S., Xu, C., Buchanan, J., Spilker, R., Dalman, R. L., Zarins, C. K., Denk, W., and Taylor, C. A. (2008). The three-dimensional micro- and nanostructure of the aortic medial lamellar unit measured using 3D confocal and electron microscopy imaging. *Matrix Biology*, 27(3):171–181.

Padala, M., Sacks, M. S., Liou, S. W., Balachandran, K., He, Z., and Yoganathan, A. P. (2010). Mechanics of the Mitral Valve Strut Chordae Insertion Region. *Journal of Biomechanical Engineering*, 132(8):081004.

Sacks, M. S., Smith, D. B., and Hiester, E. D. (1997). A Small Angle Light Scattering Device for Planar Connective Tissue Microstructural Analysis. Technical report.

Sáez, P., García, A., Peña, E., Gasser, T., and Martínez, M. (2016). Microstructural quantification of collagen fiber orientations and its integration in constitutive modeling of the porcine carotid artery. *Acta Biomaterialia*, 33:183–193.

Sun, W., Abad, A., and Sacks, M. S. (2005). Simulated Bioprosthetic Heart Valve Deformation under Quasi-Static Loading. *Journal of Biomechanical Engineering*, 127(6):905.

Xu, F., Morganti, S., Zakerzadeh, R., Kamensky, D., Auricchio, F., Reali, A., Hughes, T. J. R., Sacks, M. S., and Hsu, M.-C. (2018). A framework for designing patient-specific bioprosthetic heart valves using immersogeometric fluid-structure interaction analysis. *International Journal for Numerical Methods in Biomedical Engineering*, 34(4):e2938.

Chapter 5

Conclusive remarks

5.1 Main findings

In the context of numerical simulations of the AV biomechanics, this project was carried out to follow the research directions shared in literature in the attempt of pursuing a subject-specific numerical description on the multiscale biomechanical behavior of the AV. In the last decades FE numerical simulations techniques have become more and more reliable to study the biomechanical behavior of anatomical districts of the cardiovascular system, such as the AV, showing that these techniques are critical in understanding their function. In addition, computational simulations, either alone or in conjunction with clinical studies, have been used to define how evolving biomechanical properties drive native heart valve disease, as well as replacement valve function and performance showing not only their descriptive capabilities, but also the predictive power of this techniques. With the aim of improving these numerical techniques many groups have focused on subject-specific geometry reconstruction starting from clinical images (CT, cMRI, echocardiography), working especially on the organ length-scale description of the AV biomechanics; these improvement, which represent the current state of the art, allowed in particular for the investigation of macroscopic differences in the biomechanical behavior between physiological and pathological AV anatomies. Yet, despite these substantial advancements in simulation technology, critical heart valve pathological issues remain unsolved. This is due to the fact that the pathological mechanisms lie mainly in the behaviors of the constituent at the tissue and cell length-scale. That is, while organ level simulations can assist in understanding how the valve dynamically responds over the cardiac cycle, valve pathologies (e.g. calcific AV) are a direct result of poorly understood remodelling processes which take place at the AV tissue and cell length-scales. These processes still need to be studied, modeled mathematically and then embedded directly into organ length-scale numerical models. Thus, this project was conceived to tackle the major limitations shared among the literature, improving the state of the art by developing innovative numerical methods to study the subject-specific multiscale behavior of the AV.

First, the project focused on the development of a semi-automated algorithm to generate patient-specific image-based AV FE models for the simulation of the organ length-scale behavior of the AV, including the possibility to set the space-dependent patterns of leaflets thickness. Through this benchmark we could compare different discretization approaches to describe the AV leaflet geometry, as as described in Chapter 2. Results computed thanks to this comparison, which was lacking in literature, high-

lighted that the use of solid elements lead to a more reliable quantification of leaflet stresses and of the associated gradient through the leaflet thickness if compared to shell elements. Moreover, it was evident that leaflet stresses strongly depend on the local leaflet thickness, thus suggesting that in the context of patient-specific modeling a reliable quantification of the patient-specific tissue thickness distribution should be mandatory.

Second, we developed a FE workflow for the multiscale analysis of the AV biomechanics, starting from subject-specific anatomies. The organ length-scale models of three healthy subjects were obtained exploiting to the benchmark developed in the first part of the work (see Chapter 2), adding some slight modifications in order to obtain layer-specific thickness values for the AV leaflets. In addition, we developed an innovative way to concatenate boundary conditions, making use of alternate displacement-stress BCs in order to guide the different length-scale simulations. To the best of our knowledge this is the first multiscale AV study able to transfer subject-specific macroscopic features down to the cell-scale. Thanks to this novel workflow, we investigated the behavior of the AV leaflets at the organ, tissue and cell length scale. With the aim of studying the impact of subject-specific organ scale features on the cell-scale mechanical response, we calculated the correlation between the subject-specific leaflet extent and the circumferential and radial strain behaved by VICs at the cell length-scale; the latter suggests that the organization of matrix within the valve tissue acts to reduce direct tensile strain transfer to cells in the circumferential direction, supporting previous findings in literature. Therefore, the radial directions appears as the one which is more sensible to anatomical leaflet differences, and in which this differences are transfer to the cell environment.

Lastly, in a project carried out in collaboration with the research group of Prof. M. S. Sacks at the Willerson Center for Cardiovascular Modeling and Simulation during an exchange period at UT Austin (Austin, Texas, USA), we developed a method able to include in the organ length-scale model of the AV leaflet the collagen fiber structure. In particular, we developed a novel structural tensor method to describe fiber orientation probability density functions (ODFs), allowing for an efficient representation and tensor coordinate transformation to facilitate mapping from experimental data to NURBS based representations of AV leaflet geometry. We demonstrated the efficacy of this innovative approach starting from human derived SALS structural experimental data from normal and pathological (BAV) AV leaflets, and mapping the fiber distribution onto a paradigmatic NURBS model; however, it has to be noticed that the mapping process can

be performed also on subject-specific NURBS geometries.

To conclude, this project tackled different aspects of numerical FE modeling of AV, focusing on a subject-specific approach in three main aspects treated: the attention to the modelling and discretization aspects in the description of the AV leaflet geometry (see Chapter 2), the development of a multiscale approach going from the organ down to the cell length-scale (see Chapter 3), and the inclusion of structural tissue information in the organ length-scale models (see Chapter 4). Novel solutions were implemented to advance the current state of the art, focusing, in particular, on those technological and methodological issues that are still hampering a more comprehensive description of the biomechanical behavior of the AV through numerical simulations.

5.2 Future developments

The advancements with respect to the current state of the art achieved within this PhD project also revealed further improvements which are needed to move towards a more complete understanding of the AV behavior and in particular of the tissue remodeling processed taking place at the tissue ad cell length-scale. In particular, all the developed approaches and methods should be intended as preliminary works that laid the foundations for future investigations. As far as the AV geometry reconstruction is concerned, one important improvement should be considered in the future. The leaflet thickness distribution has been shown to have a major impact on the stress and strain distribution across the leaflet surface itself (see Chapter 2). For this reason, it should be mandatory to exploit image modalities that, differently from cMRI, allow for quantifying the subject-specific regional thickness of aortic valve leaflets, which is a key feature when quantifying aortic valve structural response. In this regard, 3D ultrasound imaging may represent a valuable option. Alternatively, age- and gender-matched, as well as class-matched (e.g. healthy valve, calcific valve, Marfan syndrome-affected valve) thickness patterns should be identified based on ex vivo measurements on cadavers or on tissue samples resected during surgical procedures. Considering the all the different algorithms implemented, a further efforts should be made in order to merge the tensor mapping description of the collagen fibers structure of Chapter 4, into the subject-specific organ-scale length subject-specific models of the multiscale FE workflow of Chapter 3. Such a comprehensive model could give more complete insights on the impact of the leaflet tissue properties onto the mechanical stimuli behaved by VICs at the cell length-scale.

List of Publications

Papers under submission on International Peer-Reviewed Journals

1. G. Rossini, A. Caimi, A. Redaelli, E. Votta **Subject-specific multi-scale modeling of aortic valve biomechanics**, under submisson on the Journal of Biomechanics and Modeling in Mechanobiology

2. W. Zhang, G. Rossini, T. Bui-Thanhc, M. S. Sacks, **The integration of structure and high-fidelity material models in heart valve simulations using machine learning**, under submission on the Journal of Computer Methods in Applied Mechanics and Engineering, special issue 2019